

# Supervised Machine Learning of High Rate GNSS Velocities for Earthquake Strong Motion Signals.

Timothy Dittmann<sup>1</sup>, Yunxiang Liu<sup>2</sup>, Y. Jade Morton<sup>3</sup>, and David Mencin<sup>3</sup>

<sup>1</sup>UNAVCO Inc.

<sup>2</sup>University of Colorado, Boulder

<sup>3</sup>University of Colorado Boulder

November 26, 2022

## Abstract

High rate Global Navigation Satellite System (GNSS) deformation time series capture a broad spectrum of earthquake strong motion signals for rapid contributions to hazard warnings and assessment, but experience regular sporadic noise that can be difficult to distinguish from true seismic signals. Previous studies developed methods for automatically detecting these signals but most rely on various external inputs to differentiate true signal from noise. In this study we generated a dataset of high rate GNSS time differenced carrier phase (TDCP) velocity time series concurrent in space and time with expected seismic surface waves from known seismic events. TDCP velocity processing has increased sensitivity relative to traditional geodetic displacement processing without requiring sophisticated corrections. We trained, validated and tested a random forest machine learning classifier. We find our supervised random forest classifier outperforms the existing detection methods in stand-alone mode by combining frequency and time domain features into decision criteria. We optimized the classifier on a balance of sensitivity and false alerting. Within a 100km epicentral radius, the classifier automatically detects 86% of events greater than MW5.0 and 98% of events greater than MW6.0. The classifier model has typical detection latencies seconds behind S-wave arrivals when run in real-time mode on “unseen” events. We conclude the performance of this model provides sufficient confidence to enable these valuable ground motion measurements to run in stand-alone mode for development of edge processing, geodetic infrastructure monitoring and inclusion in operational ground motion observations and models.

1 **Supervised Machine Learning of High Rate GNSS**  
2 **Velocities for Earthquake Strong Motion Signals.**

3 **T. Dittmann<sup>1,2</sup>, Y. Liu<sup>1</sup>, Y. Morton<sup>1</sup>, D. Mencin<sup>2</sup>**

4 <sup>1</sup>University of Colorado, Boulder  
5 <sup>2</sup>UNAVCO Inc.

6 **Key Points:**

- 7 • We assembled a labeled dataset of 5Hz GNSS velocity time series from 77 earth-  
8 quakes over nearly 20 years.  
9 • We trained a supervised random forest classifier for detecting seismic motion that  
10 outperforms existing detection methods.  
11 • Improved detection enables lightweight, high rate GNSS velocity processing to be  
12 included in operational ground motion observations.

## Abstract

High rate Global Navigation Satellite System (GNSS) deformation time series capture a broad spectrum of earthquake strong motion signals for rapid contributions to hazard warnings and assessment, but experience regular sporadic noise that can be difficult to distinguish from true seismic signals. Previous studies developed methods for automatically detecting these signals but most rely on various external inputs to differentiate true signal from noise. In this study we generated a dataset of high rate GNSS time differenced carrier phase (TDCP) velocity time series concurrent in space and time with expected seismic surface waves from known seismic events. TDCP velocity processing has increased sensitivity relative to traditional geodetic displacement processing without requiring sophisticated corrections. We trained, validated and tested a random forest machine learning classifier.

We find our supervised random forest classifier outperforms the existing detection methods in stand-alone mode by combining frequency and time domain features into decision criteria. We optimized the classifier on a balance of sensitivity and false alerting. Within a 100km epicentral radius, the classifier automatically detects 86% of events greater than  $M_W$  5.0 and 98% of events greater than  $M_W$  6.0. The classifier model has typical detection latencies seconds behind S-wave arrivals when run in real-time mode on “unseen” events. We conclude the performance of this model provides sufficient confidence to enable these valuable ground motion measurements to run in stand-alone mode for development of edge processing, geodetic infrastructure monitoring and inclusion in operational ground motion observations and models.

## Plain Language Summary

Continuously operating, high sample rate Global Navigation Satellite System (GNSS) sensors that experience ground shaking from an earthquake can provide valuable data regarding the nature of the ground motion. If this data is streamed in real-time, these observations can complement existing traditional seismic infrastructure measurements that are used for earthquake early warning or rapid ground motion assessments. However, the data from these sensors can be noisy and have non-earthquake artifacts that are difficult to tell apart from true seismic signals. In this work we used a nearly 20 year archive of high sample rate GNSS velocities occurring during known seismic events to train, validate and test a machine learning model for earthquake detection. This machine learning approach is taken from existing algorithms used for a wide variety of challenging classification problems where a label can be applied to a sample. We demonstrate that this data-driven method, without any external information, is more likely to detect these signals with less false alarms when compared to existing methods. The added confidence this algorithm provides will allow these valuable measurements to be included in operational seismic assessment and warning decision criteria.

## 1 Introduction

Real-time measurements of medium to great earthquake ground motions are vital to rapid hazard assessment and earthquake early warning (EEW) systems. Higher rate ( $\geq 1\text{Hz}$ ) continuous GNSS measurements capture dynamic motions and permanent displacements of propagating strong-motion waveforms from such events (Nicolaidis et al., 2001; Larson et al., 2003). These geodetic strong motion measurements (Larson, 2009) will rarely clip nor require double integration that leads to magnitude saturation in the near-field of larger, destructive earthquakes common to inertial velocity sensors (Bock et al., 2004; B. W. Crowell et al., 2013; Colombelli et al., 2013). Furthermore, additional material low-latency observations densify existing ground motion measurements. These

61 observations are particularly valuable when damaging seismic events occur in sparsely  
62 instrumented regions (Grapenthin et al., 2017) or when networks or infrastructure fails.

63 However, geodetic deformation timeseries are noisier than traditional inertial sensors  
64 (Melgar et al., 2020). This makes separating signal from noise challenging: signal  
65 amplitudes from the largest, most costly events can be difficult to distinguish from non  
66 geophysical events, such as filter reconvergence or signal loss of lock. Medium magnitude  
67 events, often difficult to detect above the geodetic noise floor, can be destructive or tsunami-  
68 genic. The ability to make accurate, low-latency distinction between true signals and noise  
69 in stand-alone mode, without external sensors or information, minimizes points of fail-  
70 ure and decision latency and maximizes integral network decision inputs and potential  
71 edge processing capabilities.

72 Current approaches to detect motion use variations of time domain thresholds to  
73 flatten the decision to a function of signal amplitude. Several existing approaches make  
74 use of low-pass filters similar to traditional STA/LTA seismological phase picking (Allen  
75 & Ziv, 2011; Ohta et al., 2012; Minson et al., 2014; Kawamoto et al., 2016; Goldberg &  
76 Bock, 2017) that extract static offsets for finite fault inversion but filter valuable dynam-  
77 ics information. Recent interest in peak dynamic signals (Melgar et al., 2015; Ruhl et  
78 al., 2019; Fang et al., 2020; B. W. Crowell, 2021) prompted use of unfiltered timeseries  
79 to capture peak signals for magnitude scaling laws and ground motion intensity measure-  
80 ments. These epoch-wise threshold detection methods (B. W. Crowell et al., 2009; Psi-  
81 moulis et al., 2018; Hohensinn & Geiger, 2018; Hodgkinson et al., 2020; Dittmann et al.,  
82 2022) use instantaneous measurements to estimate motion onset, but have limited “real-  
83 world” testing and mitigate high false alert rates by spatially correlating detections with  
84 nearby stations or windowing in time from seismic triggers. These processes reduce the  
85 utility of these measurements for rapid decision criteria.

86 In this work, we evaluate whether existing GNSS hardware can: more reliably detect  
87 motion signals that are 1) constellating near the ambient temporal noise floor 2) with  
88 minimal false alerting 3) in a stand-alone mode and 4) with no specific fault or network  
89 geometry. We trained a machine learning classifier on a supervised dataset of GNSS ve-  
90 locity time series concurrent in space and time with known seismic source signals. We  
91 assembled, processed and labeled a dataset of 1701 earthquake-station high rate (5Hz)  
92 time series pairs. We optimized the classifier on this dataset with applied domain knowl-  
93 edge to feature selection and feature engineering. We present the superior performance  
94 of this classifier relative to existing methods within this motivational context. We offer  
95 advantages and implications of deploying this processing and trained model at scale for  
96 network wide monitoring, with particular emphasis on the improved sensitivity and in-  
97 tegrity of stand-alone GNSS event detection without external inputs.

## 98 2 Methods

### 99 2.1 Signals of Interest

100 We define our detection domain as a binary *motion* or *no motion* state classifica-  
101 tion. A critical component of developing a robust classification model is a substantial  
102 dataset from which to train, validate and test the model. For optimal results, this dataset  
103 requires broad spectrum noise and signal samples such that the model can “learn” and  
104 generalize our classification and distinguish signal from noise. We assembled a catalog  
105 of 1701 station-event pairs from 77 events by cross referencing available 5Hz GNSS ob-  
106 servational data in the UNAVCO geodetic archive with Advanced National Seismic Sys-  
107 tem Comprehensive Earthquake Catalog (ComCat) of earthquakes greater than  $M_W 4.5$ .  
108 While 1Hz data is more readily available, this sample rate is insufficient for capturing  
109 certain event spectra (Joyner, August 1984; Smalley, 2009), such as  $\sim M_W 6.0$  events in  
110 the nearfield. For larger magnitude events it’s likely that sampling closer to 10 Hz is nec-

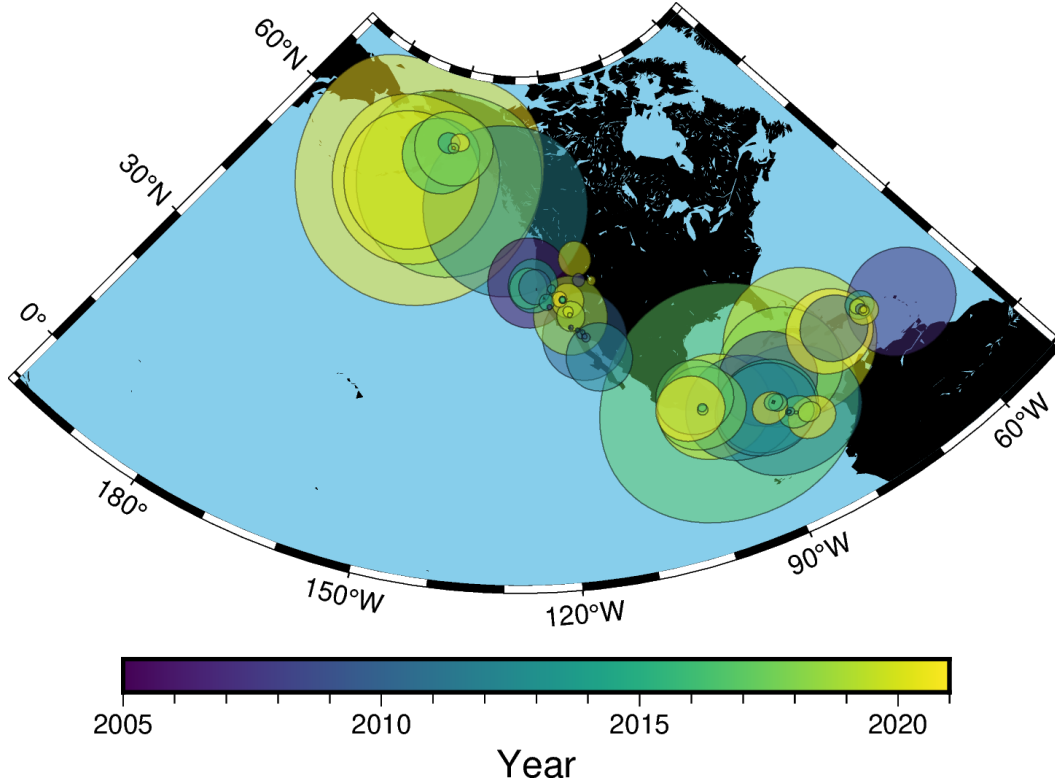


**Figure 1.** Catalog of events and radii used for this work. The number of stations used in each event is a function of the radii depicted here and the ground station network density.

111    essary to avoid aliasing (Shu et al., 2018), but we balance this design parameter with the  
 112    need for sufficiently large available datasets for training. We assigned a conservative ra-  
 113    dius of detection for each event using ambient noise estimation from Dittmann et al. (2022).  
 114    For each station-event pair within this spatial footprint, a time series window began 2  
 115    minutes prior to earthquake origin time (OT), and extends out in time as a function of  
 116    radius (Figure 1). We conservatively buffered the radius and time window to ensure the  
 117    existing model does not limit this result.

118    Current use of GNSS-derived seismic ground motion for operational EEW (Murray  
 119    et al., 2018) use precise point positioning (PPP) derived topocentric coordinates to cap-  
 120    ture dynamic waveforms or static offsets relative to a stations *a priori* position. Instead,  
 121    we align synchronous carrier phase epoch-wise changes, predicted satellite orbital veloc-  
 122    ity and line-of-sight geometry to accumulate coherent energy with respect to the shared  
 123    receiver clock drift rate and directional velocities in a local reference frame. Variations  
 124    of this geodetic processing method, known as time differenced carrier phase (TDCP) (van  
 125    Graas & Soloviev, 2004) or variometric velocities, can record co-seismic velocity wave-  
 126    forms (Grapenthin et al., 2018; Hohensinn & Geiger, 2018; B. W. Crowell, 2021) as well  
 127    as integrated over time into seismic displacement waveforms (Colosimo et al., 2011; Bran-  
 128    zanti et al., 2013; Fratarcangeli et al., 2018). We processed these 5hz measurements with  
 129    the open-source SNIVEL package (B. W. Crowell, 2021) using broadcast ephemeris and  
 130    narrow lane phase combinations. We chose TDCP over PPP because it is more sensi-  
 131    tive to motion (Fang et al., 2020; Dittmann et al., 2022), and it is “lightweight” in that  
 132    it does not require sophisticated corrections and is computationally inexpensive. From  
 133    a machine learning perspective, this could be considered a first step in our feature en-

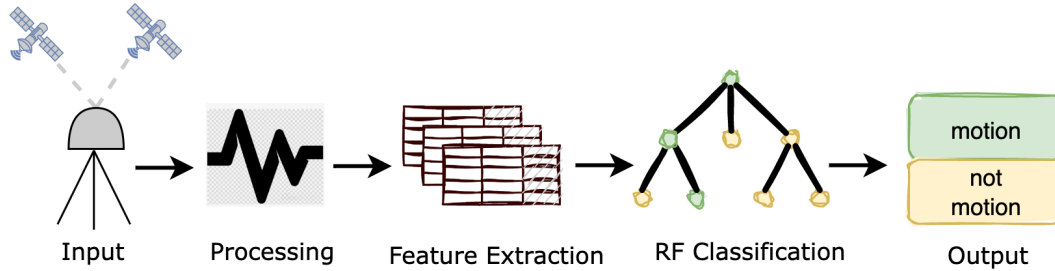


**Figure 2.** Schematic of our classification workflow: Inputs were 5Hz GPS phase measurements and broadcast ephemeris, which are processed using narrow lane combinations using SNIVEL. Target labeling combined with Feature extraction were used for training a supervised random forest classification model to predict motion classification on testing subsets.

134 geineering, or applying domain knowledge to extracting features that are correlated with  
 135 motion in observed carrier phase measurements.

## 136 2.2 Feature Engineering Pipeline

137 Data-driven supervised machine learning models are widely used in computer vi-  
 138 sion and natural language processing due to their superior accuracy for challenging clas-  
 139 sification, regression and clustering problems. Earth scientists have adopted many of these  
 140 models for geoscience research (Kong et al., 2019). Recent catalogs of historic seismic  
 141 data training sets (eg. Stanford Earthquake Data Set (Mousavi et al., 2019), INSTANCE  
 142 (Michellini et al., 2021)) have contributed to benchmarking improvements of earthquake  
 143 detection, phase picking, localization, and magnitude estimation (eg. Meier et al. (2019);  
 144 Mousavi et al. (2020); Kong et al. (2019)). These extensive labeled data sets enable so-  
 145 phisticated data-driven classifiers and deep learning models using inertial seismic data.  
 146 Several geodetic applications of machine learning algorithms have demonstrated promis-  
 147 ing results with respect to seismic processes. Crocetti et al. (2021) used a random for-  
 148 est classifier for antenna offset detection, including due to earthquake offsets, from low-  
 149 rate, 24-hour position solutions. Habboub et al. (2020) applied a neural network to co-  
 150 ordinate time series anomaly detection applicable to specific regional datasets well above  
 151 the noise floor. Dybing et al. (2021) used neural networks for earthquake detection and  
 152 Lin et al. (2021) employed deep learning used for rapid event magnitude estimation; both  
 153 of these studies used extensive synthetic displacement waveforms derived from real-world  
 154 fault geometries and real-world PPP noise models.

155 In our study, we used a random forest algorithm for our classifier (Breiman, 2001)  
 156 of GNSS velocities. Random forest is an ensemble of decision trees; a single decision tree  
 157 is a classifier where input features are split along thresholds to separate source, or root,  
 158 data from end node classifications, or leaves. An ensemble or forest of trees each vote  
 159 on the feature decision criteria to select the optimal decisions towards minimizing cor-  
 160 related noise. Due to the infrequent nature of larger magnitude earthquakes, the event  
 161 classes are naturally imbalanced but by pre-selecting specific time series of events, we  
 162 have reduced this imbalance for training (Table 1) and testing. Random forest hyper-  
 163 parameters were selected using a grid search over the number of decision trees used, the  
 164 maximum decision splits within a tree, and imbalance classification weighting strategies.

165 SNIVEL TDCP processing generates 5 Hz time series of the three topocentric ve-  
 166 locity components and the clock drift rates. From these event-station pair time series  
 167 of velocities, we generated feature sets to label for our supervised classification (Figure

**Table 1.** Distribution of classification sample labels used in training/testing datasets by component and label.

	East (n=46,778)	North (n=46,778)	Up (n=46,778)
<b>No</b>	84%	85%	97%
<b>Yes</b>	14%	13%	2%
(Maybe*)	2%	2%	<1%

\*Maybe’s excluded from training/testing

168 2). Our feature samples consisted of three directional components of 30 second windows  
 169 overlapping every 10 seconds; within these windows we included the four maximum com-  
 170 ponent norm window values, window median, window median absolute deviation and win-  
 171 dow lower frequency power spectra as features. These features and windowing allowed  
 172 our model to incorporate signal and noise amplitude in the time domain, akin to the tra-  
 173 ditional threshold approach, as well as power spectra in the frequency domain. Labels  
 174 were assigned through visual inspection as *no* or 0 for no motion, *yes* or 1 for motion,  
 175 and *maybe* for windows that we are not able to distinguish between yes or no and ex-  
 176 cluded from testing and training. Each directional component was labeled independently.  
 177 This resulted in 140,334 labels for the approximately 30 time samples for 1701 station  
 178 event pairs of three component velocity time series. We evaluated two feature extrac-  
 179 tion models. Feature set #1 was a combined array of all 3 directional components with  
 180 a single label at each window. The horizontally concatenated components resulted in  $3 \times$   
 181  $m$  features and  $n$  samples, where  $m$  is the number of features per component ( $m = 36$   
 182 in our pipeline) and  $n$  is the number of window samples. If any component was labeled  
 183 “1” for motion, the feature set #1 sample label was “1” for motion. If a *maybe* label was  
 184 present without *yes* motions on the other concurrent components, the window was ex-  
 185 cluded from training/testing. Feature set 2 included a target vector for each component  
 186 but excluded the noisier vertical signals. These vertically concatenated components re-  
 187 sulted in  $m$  features and  $2 \times n$  samples. In this extraction case any *maybe* labels were  
 188 excluded from training and testing.

189 We employed a nested cross validation approach for unbiased testing of our dataset.  
 190 We initialized 10 different folds of randomly splitting the 77 events into 90% training and  
 191 10% testing. By splitting on events we avoided “leakage” of information from our train-  
 192 ing into our testing, including correlation of seismic waveforms from any given event ob-  
 193 served across a network. By cross validating over 10 folds we minimized biasing our re-  
 194 sult by the relatively small testing subsets of events, and can quantify the ability of our  
 195 classification model to generalize for future events. Each event was observed by a dif-  
 196 ferent number of stations depending on network density and sensing radius, and each  
 197 station-event pair had differing number of time samples; consequently the feature vec-  
 198 tors of training and testing were not precisely 90/10 split in samples. In each fold, we  
 199 held the test set aside as “unseen”, and tuned our model using K-fold cross validation  
 200 (Bishop & Nasrabadi, 2007) on the remaining training set (Figure 3). We implemented  
 201 5 inner folds in our K-fold cross validation to find the best hyperparameters. This cross  
 202 validation approach allowed us to minimize overfitting the training dataset and evalu-  
 203 ate the performance of our model on unseen data as though it were running such a clas-  
 204 sifier on yet-to-occur events.

205 The traditional “accuracy” metric, or the ratio of the correctly classified labels rel-  
 206 ative to the total number of labels, of our classification will be less sensitive regardless  
 207 of optimization choices due to the infrequent events of our imbalanced classification. In-  
 208 stead, we optimized on metrics that reflect accurately classifying the infrequent events.  
 209 Precision, or positive predictive value, is equal to the number of true positives (TP) over

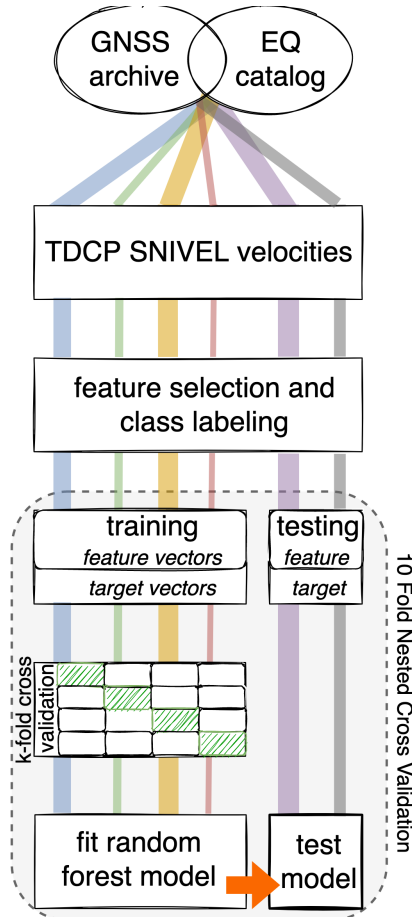


**Figure 3.** Schematic of a single fold random forest pipeline. For evaluation, we ran 10 folds of train/test splits of the 77 seismic events and report the mean and standard deviation of the test metrics to evaluate how well our features and models generalize across different testing sets.

**Table 2.** 10 fold nested cross validation results comparing Feature Set 1 is where all 3 components are combined for each window, and Feature Set 2 is where each horizontal component is tested independently.

		Feature Set #1	Feature Set #2
Precision	mean	0.79	0.73
	stdev	0.21	0.21
Recall	mean	0.71	0.67
	stdev	0.10	0.13
<b>F1</b>	mean	<b>0.73</b>	0.68
	stdev	0.14	0.14

the sum of TP and false negatives (FN).

$$Precision = \frac{TP}{TP + FP} \quad (1)$$

Recall, or sensitivity, is the number of TP over the sum of TP and false positives (FP).

$$Recall = \frac{TP}{TP + FN} \quad (2)$$

F1 is the harmonic mean of precision and recall:

$$F_1 = 2 \times \frac{precision \times recall}{precision + recall} \quad (3)$$

Here, positive denotes motion and vice versa.

Precision and recall are approximately inversely related and each is a function of our random forest decision threshold. Quantifying missed detections and false alert rates is imperative for the effectiveness of any EEW system (Minson et al., 2019). We optimized hyperparameters on F1 scores, a balance of precision and recall, but this parameter is a knob available to tune depending on societal missed detection of false alerting tolerances of a future operational system.

### 3 Results and Discussion

We evaluate the two optimal feature selection strategies and a range of random forest hyperparameters via a grid search. Given the F1 scores of our 10 fold nested cross validation approach (Table 2), our optimal model used feature set #1, with all available spatial components with a single target label to accumulate as much signal as possible towards our binary classification. Each train/test fold selected different optimal hyperparameter combinations for testing via cross validation, but the majority used 500 or 1000 decision trees, 100 decision splits and no class weighting. We used a decision threshold of 0.5 for this feature engineering approach (Figure 4) to optimize F1, a balance of precision and recall. Our mean and one standard deviation nested cross validation F1 score of  $0.73 \pm 0.14$  indicates our ability to successfully train a model using random forest. The variance in our results as a justifies our nested cross validation approach to quantify the variability in results as a function of the testing set; presumably some variability will resolve with expanded target catalogs.

#### 3.1 Feature Importance

A benefit of random forest is that individual feature importance is readily extracted from the trained model. When evaluating feature set 1, we find several aspects of the

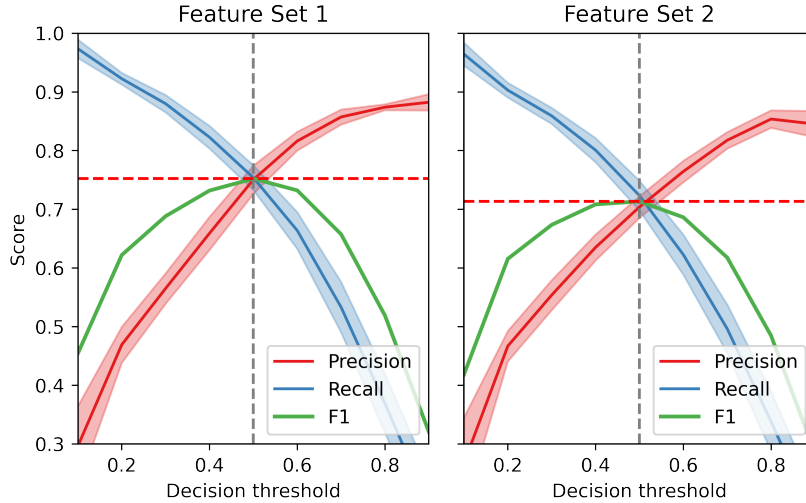


**Figure 4.** Mean precision, recall and F1 as a function of decision thresholds for the 10 fold nested cross validation evaluation. The shaded regions are the standard deviations across the 10 folds as a function of threshold. The dashed vertical lines are the maximum F1 decision threshold, with the dashed horizontal lines being the corresponding maximum F1 score.

237 feature importances that align with our domain knowledge and therefore contribute to  
 238 the explainability of our trained model. The horizontal velocity components dominate  
 239 the contribution to the model (Figure 5a). GNSS ambient noise on the vertical compo-  
 240 nent is much higher than that of the horizontal components and vertical seismic signal  
 241 amplitudes are diminished relative to horizontal motion along horizontal strike-slip fault  
 242 mechanics that are common in the spatial region of this study. These less frequent sig-  
 243 nals amidst a higher relative noise floor were harder to detect and thus contributed less  
 244 to the empirical classification model. Within a horizontal component, the lower frequency  
 245 spectral features had the most influence (Figure 5b). The most important frequency bins  
 246 were between 15-6 second periods, aligned with the prevalent frequencies of seismic sur-  
 247 face waves. Our 5Hz sampling, as compared to lower rates, boosted the detectability around  
 248 the noise floor, and avoided corner frequency aliasing of certain magnitudes. The time  
 249 domain features contributed to the model, albeit much less than the lower frequency spec-  
 250 tral content. After initial evaluation, we removed higher frequency power spectra from  
 251 our features; these are logically “noise” in our system and were not contributing to clas-  
 252 sification. Altogether, these feature importances illustrate a key attribute of such a ma-  
 253 chine learning approach: combining features in an explainable way into an effective de-  
 254 cision process.

### 255 3.2 Comparison with Existing Methods

256 A critical performance indicator is evaluating how our classification model performs  
 257 over a range of test events relative to existing threshold approaches. Logic was applied  
 258 to map existing continuous epoch-wise time domain threshold detection to our 30 sec-  
 259 ond overlapping window target labels. For a threshold method comparison similar to the  
 260 approach of Hodgkinson et al. (2020) and Dittmann et al. (2022), we estimated the noise  
 261 threshold in the 2 minute window prior to seismic origin time. Hodgkinson et al. (2020)  
 262 characterized the stand-alone sensitivity of detection using ambient noise antecedent to  
 263 an event as a Gaussian heuristic threshold. Dittmann et al. (2022) approximated the 2  
 264 minute window of ground velocities as a non central chi-squared (NCX2) distribution

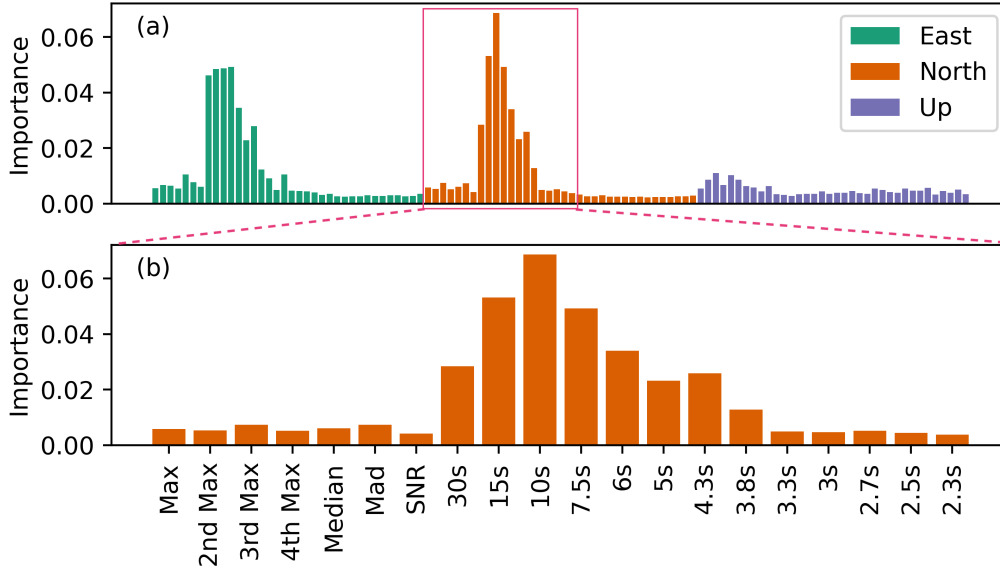


**Figure 5.** Feature importances from feature set #1 testing. 5a is the distribution of the importances across the horizontally concatenated, three spatial components. 5b is a close up of the east component, with the features labeled across the x axis. From the left, the first 6 of each component are time domain features (max, min, mad) within the 30 second windows; the next 15 are the power spectra from a periodogram of the 30 second 5Hz data, increasing in frequency from left to right. For reference, the periods are indicated.

265 with 3 degrees of freedom, and then set the 0.995 confidence level value of this distri-  
 266 bution as a noise floor approximation. Any three dimensional GV magnitude above this  
 267 noise threshold after this window is considered an event, and evaluated on whether it  
 268 falls within a window labeled motion or not. RT-Shake (Psimoulis et al., 2018) evolved  
 269 the previous geodetic STA/LTA algorithms (Allen & Ziv, 2011; Ohta et al., 2012) by dif-  
 270 ferencing instantaneous measurements from 80 epoch moving averages and then related  
 271 these values to a moving window noise threshold estimate set to three times the stan-  
 272 dard error of the previous 80 epochs. This method was run on each component indepen-  
 273 dently, with a single boolean for the presence of motion on any component, and each sam-  
 274 ple window assigned a boolean based on the presence of any motion. The Dittmann et  
 275 al. (2022) implementation of the threshold window in time was based upon S-Wave speeds  
 276 (B. W. Crowell et al., 2013), and Psimoulis et al. (2018) modified STA/LTA correlated  
 277 with surrounding stations to minimize false alerts; we did not add this logic so that we  
 278 could simulate running as a stand-alone instrument.

279 The mean precision, F1 and accuracy from our 10 fold test of our random forest  
 280 classifier outperforms the existing threshold approaches (Figure 6). In the threshold ap-  
 281 proach, recall is higher than the random forest classifier; given the large number of false  
 282 positives that this method triggers, we believe this value is boosted by chance noise trig-  
 283 gers occurring in windows of true motion triggering the motion boolean. This further  
 284 demonstrates the value of optimizing on F1 as a balance of precision and recall to re-  
 285 duce biasing one decision criteria. Precision is low for both the threshold method and  
 286 the STA/LTA, but for different reasons; while the precision values (Equation 1) are nearly  
 287 identical, the threshold method suffers from a relatively high amount of false positives,  
 288 whereas the STA/LTA method low score is due to a lower amount of true positives. This

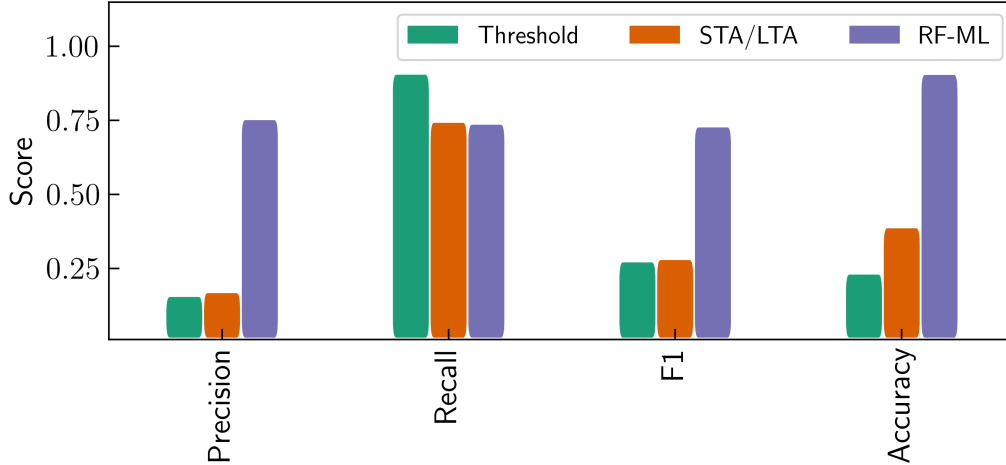


**Figure 6.** Performance metrics for 3 methods in stand-alone mode without external triggers or correlation. Threshold is the NCX2-995 approach used by Dittmann et al. (2022) that thresholds the noise based upon the 0.995 significance of a non-central chi-squared distribution of the ambient noise. STA/LTA is based on Psimoulis et al. (2018) GNSS motion detection modified STA/LTA algorithm. RF-ML is the method presented in the work here. Optimizing on F1 in this study allows us to balance missed detections (recall) with false alerts (precision); given the amount of false alerts of the Threshold and STA/LTA, the higher recall score could be a result of regular noise triggering events.

289 discrepancy is evident in the accuracy scores, where the STA/LTA outperforms the thresh-  
 290 hold approach. False positives would be decreased if using additional external informa-  
 291 tion as their authors’ suggest, such as stricter time window approaches and correlating  
 292 in space within networks. Such an approach would also likely improve the random fore-  
 293 st classifiers performance but limit the utility of a stand-alone detection node. Spatio-  
 294 temporal information could be incorporated into future network decision criteria.

### 295 3.3 Edge Sensitivity Detection

296 Detecting the largest amplitude velocity waveforms relative to ambient noise does  
 297 not present a significant challenge outside of mitigating false alerting from sporadic out-  
 298 liers (Figure 7), with a 98% true positive rate of events greater than  $M_W 6.0$  and less than  
 299 100km radius. The random forest classifier’s balance of improved false alerting relative  
 300 to thresholds and improved sensitivity relative to the STA/LTA is evident for these high-  
 301 est seismic risks. To further investigate the random forest model performance we eval-  
 302 uate detecting signals closer to the noise floor. For simplicity, we bin seismic motion edge  
 303 case detection into two distinct classes in what is a continuous distribution: large mag-  
 304 nitude event seismic motion detection in the far field, and smaller magnitude events de-  
 305 tected in the nearfield.

306 In the relative nearfield, much of the seismic energy passes through a station in shorter  
 307 duration, varied frequency signals. Earthquake focal depth and fault slip distribution in  
 308 time and space can significantly vary these waveforms as observed. Critically, the wave-  
 309 form signatures can appear similar to those of non geophysical processing outliers which  
 310 we wish to ignore for this classification. Most existing STA/LTA methods filter these noise  
 311 signals but also these valuable higher frequency dynamics. In the previous threshold meth-

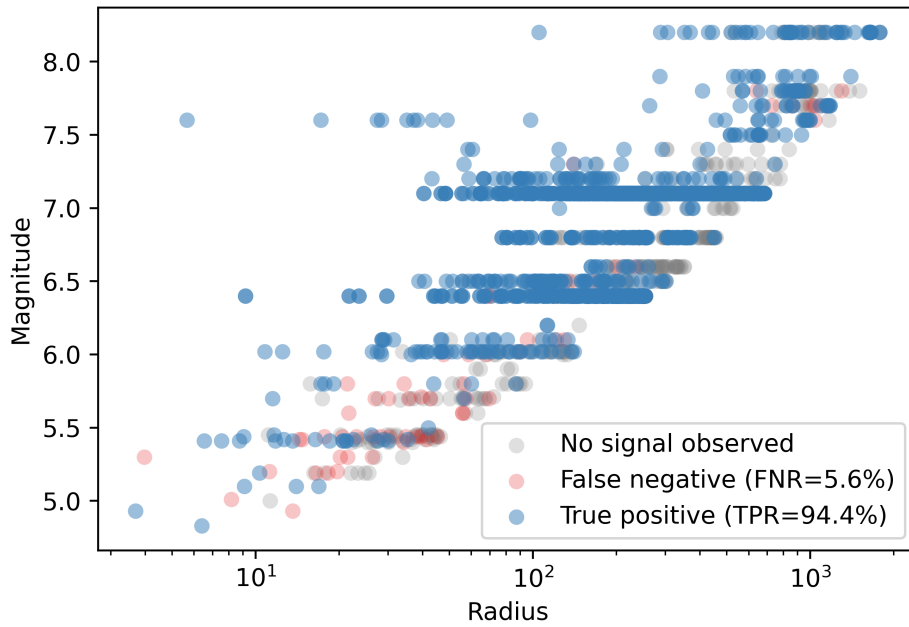


**Figure 7.** Performance of Random forest model developed in the work here across the entire event catalog. We reduce detection of events to a single binary for the figure. In this, each event is evaluated in a “test” split during the nested validation pipeline. This approach ensures each result depicted was evaluated as “unseen” relative to the best fit model from the training subset, and therefore representative of our model’s future performance.

312 ods, detection of these edge cases was a function of the ambient noise level, with low pre-  
 313 cision resulting (Figure 6) as a result of a high false positive rate. Our classifier has far  
 314 less false alerts than the threshold approach in these signals, but nevertheless still presents  
 315 the hardest detection domain for our classifier, evident in the missed detections of Fig-  
 316 ure 7 of events less than  $M_W 6.0$ . Figure 8 is an example of a smaller magnitude event  
 317 ( $M_W 5.4$ ) in the relative nearfield (21km). In the top 4 panels it is evident that accurately  
 318 detecting such an event using the threshold or modified STA/LTA approach is difficult;  
 319 not only does the true signal barely exceed the noise floor, but there are numerous false  
 320 alerts using both methods. The random forest classifier captures each labeled motion  
 321 window in addition to “ignoring” the spurious signal around 100s OT that triggers all  
 322 of the other methods evaluated.

323 The sensitivity of GNSS to long period surface waves are apparent at relatively great  
 324 radii in the 5 hz TDCP velocity time series (Figure 7). The model detects teleseismic  
 325 surface waves in unfiltered GNSS velocities at 1780km epicentral radius in real-time with  
 326 no external corrections; Figure 9 provides an example of this detection. In Figure 9, the  
 327 amplitude of the ground velocity magnitude of these long period signals is insufficient  
 328 to cross the traditional noise threshold, and for that same noise threshold there are many  
 329 false alerts. The modified STA/LTA RT-Shake approach does not identify the major-  
 330 ity of the long period waves either, while the random forest classifier in the bottom panel  
 331 only misses the first window.

### 332 3.4 Decision Latency

333 Delay in alerting is critical to EEW. While our model is trained, tested, and val-  
 334 idated on overlapping windows every 10 seconds, we evaluate running the model at once  
 335 per second, the current US EEW (ShakeAlert (Murray et al., 2018)) geodetic input rate  
 336 (Figure 10). On testing data not used in model training, we find a delay relative to the  
 337 P-wave ( $\sim 3$  seconds average at 10km) exists in the current approach. GNSS velocities  
 338 using this current approach cannot reliably be used for initial phase (P-wave) picking,  
 339 but can rapidly contribute to ground motion models or peak motion scaling laws (Fang  
 340 et al., 2020). Given the feature importances of the classifier (Fig 5), delays are a result  
 341 of coseismic energy organizing into surface waves which are confidently detected by the  
 342 model. These are the signals we were visibly able to distinguish in labeling. Variance in  
 343 delays in the near field are likely due to inherent limitations of modeling rupture as a  
 344 point source at proximal locations (Goldberg et al., 2021). It is worth repeating that this  
 345 assessment uses no external input or seismic triggering.

### 346 3.5 Ambient Noise Dataset

347 In addition to evaluating the performance within the bespoke event data sets, we  
 348 also evaluate the performance of the method during a period of quiescence. We randomly  
 349 selected 30 spatially distributed stations that supported 5 Hz downloads one hour in ad-  
 350 vance of the 2019  $M_W 6.4$  Ridgecrest Earthquake. We processed a 60 minute window to  
 351 be representative of ambient noise: there were no events  $> M 4.0$  in the USGS comcat cat-  
 352 alog, space weather indices were calm (Ap 4 nT) and all other sources of noise (signal  
 353 multipath, oscillators, etc) were included. We assigned labels of *no motion* to all target  
 354 vectors associated with feature extraction, and thus can evaluate ambient noise perfor-  
 355 mance, or false alarm rate (Figure 11). We applied the previously trained classifier model  
 356 once per second, to simulate running such a model in real-time mode.

357 Overall, the random forest classifier is less susceptible to spurious signals or out-  
 358 liers over the window tested than the threshold and STA/LTA approaches. As expected,  
 359 the two threshold models are the most susceptible to false alerting; evident from the pre-  
 360 cision metric reported in Figure 6. The variations present in the random forest approach  
 361 suggest that the current model has some station/time dependence not aligned with the

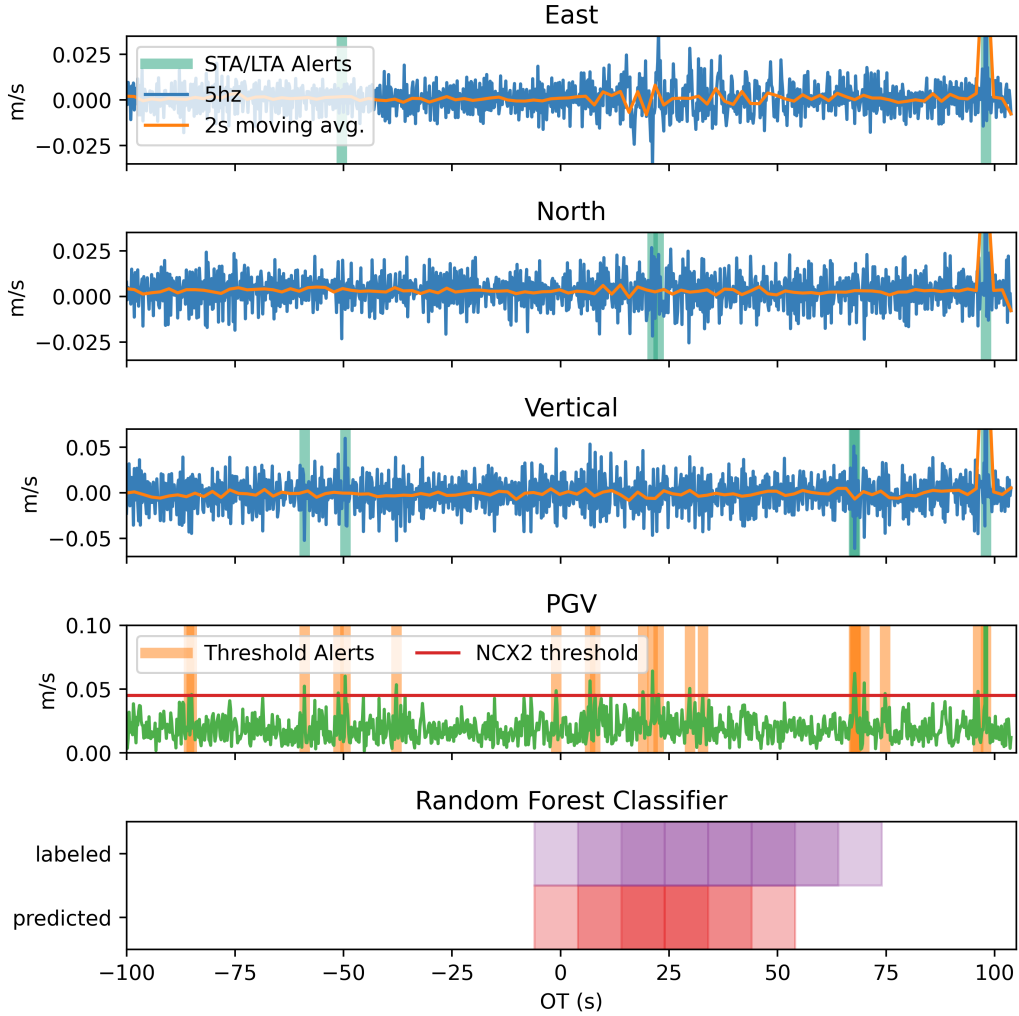


**Figure 8.** Velocity and detection time series from P507 observing a M5.41 at 21km epicentral radius. In the top 3 panels, we include a downsampled running mean so that the reader may readily visualize the lower frequency surface waves passing through. The teal vertical lines are alerts from the STA/LTA classifier (Psimoulis et al., 2018) on each component. The fourth panel green timeseries is the 3 component GV; the red horizontal line is the sensitivity threshold of a 0.995 non central chi squared (ncx2) noise model (Dittmann et al., 2022)), with orange vertical lines indicating a potential alert where GV greater than the threshold. The fifth panel is a comparison of the labeled feature set 1 for this event-station pair in purple, and the results of the model prediction in red. Shading is used to distinguish overlaps. This event-station pair prediction is extracted from the test or unseen event collection.

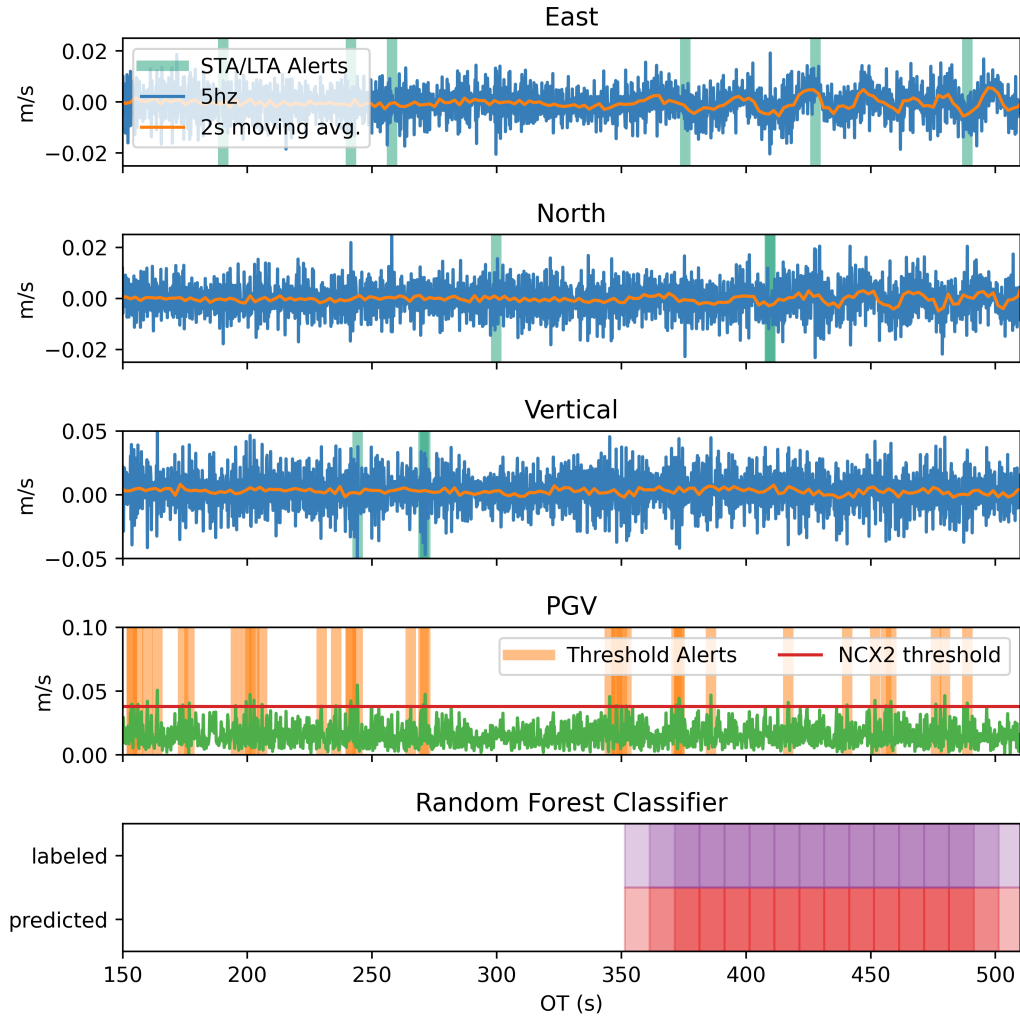


**Figure 9.** Velocity and detection time series from Station AB18 observing a  $M_W 7.9$  from  $\sim 1400$  km epicentral radius. In the top 3 panels, we include a downsampled running mean so that the reader may readily visualize the lower frequency surface waves passing through, but these are not used in the models. The teal vertical lines are alerts from the STA/LTA classifier (Psimoulis et al., 2018) on each component. The fourth panel green timeseries is the 3 component GV; the red horizontal line is the sensitivity threshold of a 0.995 non central chi squared (ncx2) noise model (Dittmann et al., 2022), with orange vertical lines indicating a potential alert where GV greater than the threshold. The fifth panel is a comparison of the labeled feature set 1 for this event-station pair in purple, and the results of the model prediction in red. Shading is used to distinguish overlaps. This event-station pair prediction is extracted from the test or unseen event collection.

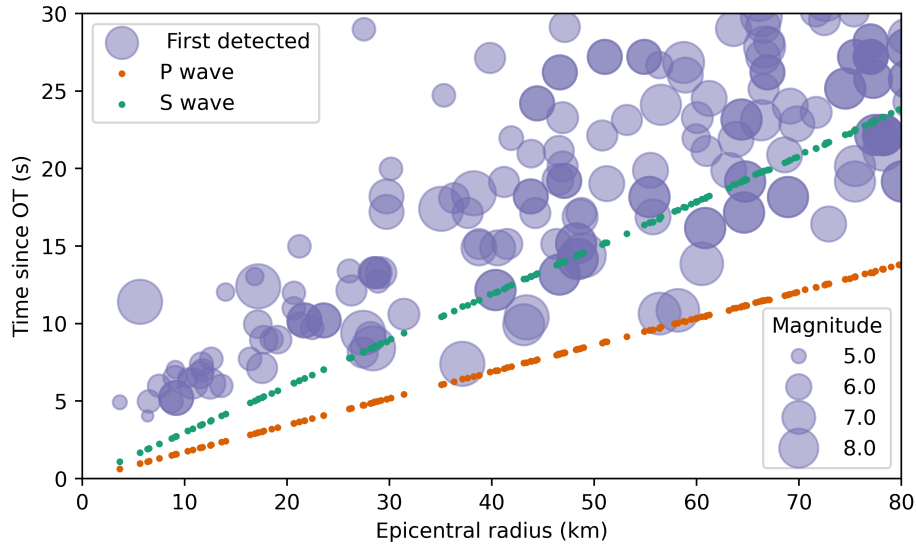


**Figure 10.** Time of first detection of all individual event-station pairs within 80km epicentral radius relative to earthquake origin time (OT) as a function of radius. Green dots are the estimated P- and S-wave arrivals at the event-station pairs used in this study shown for reference. Purple circles are centered on the time of first detection after the OT, where the diameter is scaled to the event magnitude. These results are from the classifier run at 1Hz on unseen testing sets to simulate a real-time operational mode.

362 variations of other methods. Inclusion of larger noise training datasets into our detec-  
 363 tion classifier and possibly data augmentation techniques would likely be beneficial to-  
 364 wards training on the widest variety of noise scenarios.

## 365 4 Conclusion

366 We applied an existing machine learning algorithm and sample splitting pipeline  
 367 techniques to training, validating and testing a seismic motion detection classifier from  
 368 5Hz TDCP GNSS velocities. We leveraged nearly 20 years of 5Hz GNSS data archives  
 369 for training a classification model that outperforms existing threshold approaches for de-  
 370 tecting motion in stand-alone mode. The classifier combines time domain and frequency  
 371 domain features to match the sensitivity of the threshold method without the false alerts,  
 372 and matches the minimal false alerting of the STA/LTA with improved sensitivity. Given  
 373 the agreement that GNSS velocities have with existing ground motion models (B. Crow-  
 374 ell et al., 2022) and the increased confidence in separating signal from noise demonstrated  
 375 here, these GNSS velocities can operationally contribute to ground motion measurements.  
 376 The alert latency of this current model does not match the sensitivity of existing inertial  
 377 infrastructure. A complementary approach using the information available at the  
 378 time, including lowest latency p-wave characterization from inertial sensors and unsat-  
 379 urated velocity estimation from GNSS provides an optimal solution for existing dense  
 380 multi-sensor networks. For less dense networks of either sensor type, it is more critical  
 381 to establish a decision criteria for balancing timing, noise and accuracy of these indepen-  
 382 dent observation systems. Further investigation of integrating the processing and clas-  
 383 sifying approach of this manuscript with the sensitivity of co-located MEMS sensors (Goldberg  
 384 & Bock, 2017) would advantageously overlap seismic and geodetic traditional boundaries.

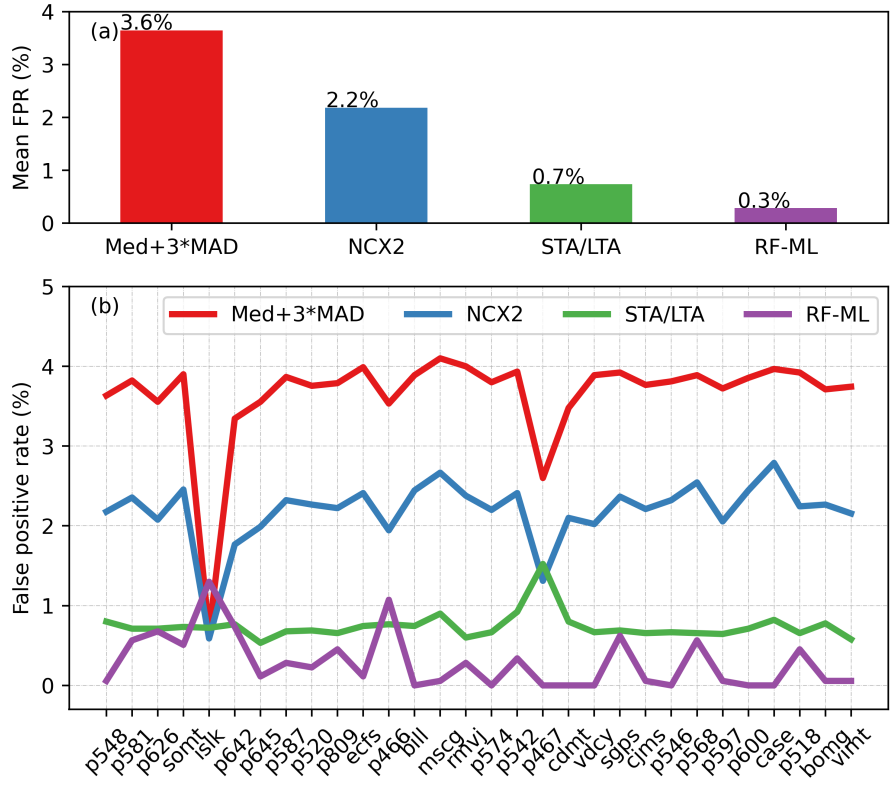


**Figure 11.** Panel (a) is mean false positive rates (FPR) from 30 randomly selected, spatially distributed, TDCP 5Hz velocities during the same 60 minute time window (1600-1700 4 July 2019). Methods include: median plus 3 times the median absolute deviation threshold of Hodgkinson et al. (2020), non-central chi square of Dittmann et al. (2022) NCX2 using alpha value of 0.995, the modified STA/LTA implemented by Psimoulis et al. (2018) and the random forest machine learning classifier developed in this work (RF-ML). Panel (b) is the distribution by station of each method.

385 Current 5 Hz GNSS observation data streams are too verbose for many bandwidth  
 386 limited remote hardware; this presents an exciting opportunity for edge processing at  
 387 potentially much higher rates (Shu et al., 2018), or experimental lean 5 Hz carrier phase  
 388 data streams. Our method presented here does not use a sophisticated machine learn-  
 389 ing model, yet has improved detection relative to existing approaches; much improve-  
 390 ment remains, especially with expanded datasets across global networks and/or synthe-  
 391 tics or data augmentation for training, validation and testing of neural networks and deep  
 392 learning models.

393 With an expanding availability and access to real-time GNSS streaming networks,  
 394 the seismological community stands to benefit from this signal of opportunity for rapid  
 395 ground motion detection for earthquake and tsunami source characterization. Further-  
 396 more, the vast industry of GNSS position, navigation and timing users catalyzing the  
 397 expansion of these GNSS real-time networks will benefit from improved automated alert-  
 398 ing of reference station motion onset. Future work will include integrating this classi-  
 399 fier amongst existing and future automated GNSS carrier phase disturbance character-  
 400 ization methods, including space weather disturbances (Jiao et al., 2017), oscillator anoma-  
 401 lies (Liu & Morton, 2022), radio frequency interference and signal multipath.

## 402 5 Open Research

403 The 5Hz GNSS data used for TDCP processing in the study are available from the  
 404 Geodetic Facility for the Advancement of Geoscience (GAGE) Global Navigation Satel-  
 405 lite Systems (GNSS) archives as maintained by UNAVCO, Inc. The data are available  
 406 in RINEX (v.2.11) format at [https://data.unavco.org/archive/gnss/highrate/5-  
 407 -Hz/rinex/](https://data.unavco.org/archive/gnss/highrate/5-Hz/rinex/). Earthquake depths, locations, and magnitudes came from the Advanced  
 408 National Seismic System (ANSS) Comprehensive Catalog of Earthquake Events and Prod-  
 409 ucts (<https://earthquake.usgs.gov/data/comcat/>). Arrival times are calculated us-  
 410 ing the iasp91 velocity model as implemented by Incorporated Research Institutions for  
 411 Seismology (IRIS) Web Services (<http://service.iris.edu/irisws/traveltime/>).  
 412 SNIVEL code used for TDCP velocity processing is developed openly at [https://github  
 413 .com/crowellbw/SNIVEL](https://github.com/crowellbw/SNIVEL) (Accessed December 2021)(B. W. Crowell, 2021). SNIVEL 5Hz  
 414 velocity timeseries used in this study are preserved at [https://doi.org/10.5281/zenodo  
 415 .6588601](https://doi.org/10.5281/zenodo.6588601). Version 1.0.1 of the scikit-learn software used for random forest classification  
 416 is preserved at <https://doi.org/10.5281/zenodo.5596244> and developed openly at  
 417 <https://github.com/scikit-learn/scikit-learn>. (Pedregosa et al., 2011) Version  
 418 v0.5.0 of PyGMT used for generating the map is preserved at [https://doi.org/10.5281/  
 419 zenodo.5607255](https://doi.org/10.5281/zenodo.5607255) and developed openly at [https://github.com/GenericMappingTools/  
 420 pygmt](https://github.com/GenericMappingTools/pygmt)(Wessel et al., 2019)

## 421 Acknowledgments

422 This material is based on services provided by the GAGE Facility, operated by UNAVCO,  
 423 Inc., with support from the National Science Foundation, the National Aeronautics and  
 424 Space Administration, and the U.S. Geological Survey under NSF Cooperative Agree-  
 425 ment EAR-1724794. High-rate processing and and machine learning for geoscience and  
 426 hazards research is supported by NSF OAC-1835791

## 427 References

- 428 Allen, R. M., & Ziv, A. (2011). Application of real-time GPS to earthquake  
 429 early warning. *Geophysical Research Letters*, *38*(16), n/a–n/a. doi:  
 430 10.1029/2011gl047947
- 431 Bishop, C. M., & Nasrabadi, N. M. (2007). Pattern Recognition and Machine Learn-  
 432 ing. *J. Electronic Imaging*, *16*, 049901.

- 433 Bock, Y., Prawirodirdjo, L., & Melbourne, T. I. (2004). Detection of arbitrarily  
434 large dynamic ground motions with a dense high-rate GPS network. *Geophysical*  
435 *Research Letters*, *31*(6), n/a–n/a. doi: 10.1029/2003gl019150
- 436 Branzanti, M., Colosimo, G., Crespi, M., & Mazzoni, A. (2013). Gps near-real-  
437 time coseismic displacements for the great tohoku-oki earthquake. *IEEE Geo-*  
438 *science and Remote Sensing Letters*, *10*(2), 372–376. doi: 10.1109/LGRS.2012  
439 .2207704
- 440 Breiman, L. (2001). Random Forests. *Machine Learning*, *45*(1), 5–32. doi: 10.1023/  
441 a:1010933404324
- 442 Colombelli, S., Allen, R. M., & Zollo, A. (2013). Application of real-time GPS  
443 to earthquake early warning in subduction and strike-slip environments.  
444 *Journal of Geophysical Research: Solid Earth*, *118*(7), 3448–3461. doi:  
445 10.1002/jgrb.50242
- 446 Colosimo, G., Crespi, M., & Mazzoni, A. (2011). Real-time GPS seismology with a  
447 stand-alone receiver: A preliminary feasibility demonstration. *Journal of Geo-*  
448 *physical Research: Solid Earth (1978–2012)*, *116*(B11), n/a–n/a. doi: 10.1029/  
449 2010jb007941
- 450 Crocetti, L., Schartner, M., & Soja, B. (2021). Discontinuity Detection in GNSS  
451 Station Coordinate Time Series Using Machine Learning. *Remote Sensing*,  
452 *13*(19), 3906. doi: 10.3390/rs13193906
- 453 Crowell, B., DeGrande, J., Dittmann, T., & Ghent, J. (2022). *Validation of peak*  
454 *ground velocities recorded on very-highrate gnss against nga-west2 ground*  
455 *motion models*. (Seismological Society of America Annual Meeting 2022)
- 456 Crowell, B. W. (2021). Near-Field Strong Ground Motions from GPS-Derived Veloc-  
457 ities for 2020 Intermountain Western United States Earthquakes. *Seismological*  
458 *Research Letters*, *92*(2A), 840–848. doi: 10.1785/0220200325
- 459 Crowell, B. W., Bock, Y., & Squibb, M. B. (2009). Demonstration of Earth-  
460 quake Early Warning Using Total Displacement Waveforms from Real-  
461 time GPS Networks. *Seismological Research Letters*, *80*(5), 772–782. doi:  
462 10.1785/gssrl.80.5.772
- 463 Crowell, B. W., Melgar, D., Bock, Y., Haase, J. S., & Geng, J. (2013). Earthquake  
464 magnitude scaling using seismogeodetic data. *Geophysical Research Letters*,  
465 *40*(23), 6089–6094. doi: 10.1002/2013gl058391
- 466 Dittmann, T., Hodgkinson, K., Morton, J., Mencin, D., & Mattioli, G. S. (2022).  
467 Comparing Sensitivities of Geodetic Processing Methods for Rapid Earthquake  
468 Magnitude Estimation. *Seismological Research Letters*, *93*(3), 1497–1509. doi:  
469 10.1785/0220210265
- 470 Dybing, S., Melgar, D., Thomas, A., Hodgkinson, K., & Mencin, D. (2021). *Detect-*  
471 *ing earthquakes in noisy real-time gnss data with machine learning*. Retrieved  
472 from `\url{https://agu.confex.com/agu/fm21/meetingapp.cgi/Paper/`  
473 `820583}` (American Geophysical Union Fall Meeting 2021)
- 474 Fang, R., Zheng, J., Geng, J., Shu, Y., Shi, C., & Liu, J. (2020). Earthquake  
475 Magnitude Scaling Using Peak Ground Velocity Derived from High-Rate  
476 GNSS Observations. *Seismological Research Letters*, *92*(1), 227–237. doi:  
477 10.1785/0220190347
- 478 Fratarcangeli, F., Savastano, G., D’Achille, M. C., Mazzoni, A., Crespi, M., Riguzzi,  
479 F., ... Pietrantonio, G. (2018). Vadase reliability and accuracy of real-time  
480 displacement estimation: Application to the central italy 2016 earthquakes.  
481 *Remote Sensing*, *10*(8). Retrieved from `https://www.mdpi.com/2072-4292/`  
482 `10/8/1201` doi: 10.3390/rs10081201
- 483 Goldberg, D. E., & Bock, Y. (2017). Self-contained local broadband seismogeode-  
484 tic early warning system: Detection and location. *Journal of Geophysical Re-*  
485 *search: Solid Earth*, *122*(4), 3197–3220. doi: 10.1002/2016jb013766
- 486 Goldberg, D. E., Melgar, D., Hayes, G. P., Crowell, B. W., & Sahakian, V. J. (2021,  
487 08). A Ground-Motion Model for GNSS Peak Ground Displacement. *Bulletin*

- 488       of the *Seismological Society of America*, 111(5), 2393-2407. Retrieved from  
 489       <https://doi.org/10.1785/0120210042> doi: 10.1785/0120210042
- 490       Grapenthin, R., West, M., & Freymueller, J. (2017). The Utility of GNSS for Earth-  
 491       quake Early Warning in Regions with Sparse Seismic Networks The Utility  
 492       of GNSS for Earthquake Early Warning in Regions with Sparse Seismic Net-  
 493       works. *Bulletin of the Seismological Society of America*, 107(4), 1883–1890.  
 494       doi: 10.1785/0120160317
- 495       Grapenthin, R., West, M., Tape, C., Gardine, M., & Freymueller, J. (2018). Single-  
 496       Frequency Instantaneous GNSS Velocities Resolve Dynamic Ground Motion of  
 497       the 2016 Mw 7.1 Iniskin, Alaska, Earthquake. *Seismological Research Letters*,  
 498       89(3), 1040–1048. doi: 10.1785/0220170235
- 499       Habboub, M., Psimoulis, P. A., Bingley, R., & Rothacher, M. (2020). A Multiple  
 500       Algorithm Approach to the Analysis of GNSS Coordinate Time Series for De-  
 501       tecting Geohazards and Anomalies. *Journal of Geophysical Research: Solid*  
 502       *Earth*, 125(2). doi: 10.1029/2019jb018104
- 503       Hodgkinson, K. M., Mencin, D. J., Feaux, K., Sievers, C., & Mattioli, G. S. (2020).  
 504       Evaluation of Earthquake Magnitude Estimation and Event Detection Thresh-  
 505       olds for Real-Time GNSS Networks: Examples from Recent Events Captured  
 506       by the Network of the Americas. *Seismological Research Letters*, 91(3), 1628–  
 507       1645. doi: 10.1785/0220190269
- 508       Hohensinn, R., & Geiger, A. (2018). Stand-Alone GNSS Sensors as Velocity Seis-  
 509       mometers: Real-Time Monitoring and Earthquake Detection. *Sensors*, 18(11),  
 510       3712. doi: 10.3390/s18113712
- 511       Jiao, Y., Hall, J. J., & Morton, Y. T. (2017). Performance Evaluation of an Auto-  
 512       matic GPS Ionospheric Phase Scintillation Detector Using a Machine-Learning  
 513       Algorithm. *Navigation*, 64(3), 391–402. doi: 10.1002/navi.188
- 514       Joyner, W. (August 1984). A SCALING LAW FOR THE SPECTRA OF LARGE  
 515       EARTHQUAKES. *Bulletin of the Seismological Society of America*, 74(4),  
 516       1167–1188.
- 517       Kawamoto, S., Hiyama, Y., Ohta, Y., & Nishimura, T. (2016). First result  
 518       from the GEONET real-time analysis system (REGARD): the case of the  
 519       2016 Kumamoto earthquakes. *Earth, Planets and Space*, 68(1), 190. doi:  
 520       10.1186/s40623-016-0564-4
- 521       Kong, Q., Trugman, D. T., Ross, Z. E., Bianco, M. J., Meade, B. J., & Gerstoft,  
 522       P. (2019). Machine Learning in Seismology: Turning Data into Insights.  
 523       *Seismological Research Letters*, 90(1), 3–14. doi: 10.1785/0220180259
- 524       Larson, K. M. (2009). GPS seismology. *Journal of Geodesy*, 83(3-4), 227–233. doi:  
 525       10.1007/s00190-008-0233-x
- 526       Larson, K. M., Bodin, P., & Gombert, J. (2003). Using 1-Hz GPS Data to Measure  
 527       Deformations Caused by the Denali Fault Earthquake. *Science*, 300(5624),  
 528       1421–1424. doi: 10.1126/science.1084531
- 529       Lin, J., Melgar, D., Thomas, A. M., & Searcy, J. (2021). Early Warning for Great  
 530       Earthquakes From Characterization of Crustal Deformation Patterns With  
 531       Deep Learning. *Journal of Geophysical Research: Solid Earth*, 126(10). doi:  
 532       10.1029/2021jb022703
- 533       Liu, Y., & Morton, Y. J. (2022). Improved Automatic Detection of GPS Satel-  
 534       lite Oscillator Anomaly using a Machine Learning Algorithm. *NAVI-*  
 535       *GATION: Journal of the Institute of Navigation*, 69(1), navi.500. doi:  
 536       10.33012/navi.500
- 537       Meier, M., Ross, Z. E., Ramachandran, A., Balakrishna, A., Nair, S., Kundzicz, P.,  
 538       ... Yue, Y. (2019). Reliable Real-Time Seismic Signal/Noise Discrimination  
 539       With Machine Learning. *Journal of Geophysical Research: Solid Earth*, 124(1),  
 540       788–800. doi: 10.1029/2018jb016661
- 541       Melgar, D., Crowell, B. W., Geng, J., Allen, R. M., Bock, Y., Riquelme, S., ...  
 542       Ganas, A. (2015). Earthquake magnitude calculation without saturation from

- 543 the scaling of peak ground displacement. *Geophysical Research Letters*, 42(13),  
544 5197–5205. doi: 10.1002/2015gl064278
- 545 Melgar, D., Crowell, B. W., Melbourne, T. I., Szeliga, W., Santillan, M., & Scrivner,  
546 C. (2020). Noise Characteristics of Operational Real-Time High-Rate GNSS  
547 Positions in a Large Aperture Network. *Journal of Geophysical Research: Solid*  
548 *Earth*, 125(7). doi: 10.1029/2019jb019197
- 549 Michelini, A., Cianetti, S., Gaviano, S., Giunchi, C., Jozinović, D., & Lauciani, V.  
550 (2021). INSTANCE – the Italian seismic dataset for machine learning. *Earth*  
551 *System Science Data*, 13(12), 5509–5544. doi: 10.5194/essd-13-5509-2021
- 552 Minson, S. E., Baltay, A. S., Cochran, E. S., Hanks, T. C., Page, M. T., McBride,  
553 S. K., . . . Meier, M.-A. (2019). The Limits of Earthquake Early Warning  
554 Accuracy and Best Alerting Strategy. *Scientific Reports*, 9(1), 2478. doi:  
555 10.1038/s41598-019-39384-y
- 556 Minson, S. E., Murray, J. R., Langbein, J. O., & Gomberg, J. S. (2014). Real-time  
557 inversions for finite fault slip models and rupture geometry based on high-rate  
558 GPS data. *Journal of Geophysical Research: Solid Earth*, 119(4), 3201–3231.  
559 doi: 10.1002/2013jb010622
- 560 Mousavi, S. M., Ellsworth, W. L., Zhu, W., Chuang, L. Y., & Beroza, G. C. (2020).  
561 Earthquake transformer—an attentive deep-learning model for simultaneous  
562 earthquake detection and phase picking. *Nature Communications*, 11(1), 3952.  
563 doi: 10.1038/s41467-020-17591-w
- 564 Mousavi, S. M., Sheng, Y., Zhu, W., & Beroza, G. C. (2019). STanford EArthquake  
565 Dataset (STEAD): A Global Data Set of Seismic Signals for AI. *IEEE Access*,  
566 7, 179464–179476. doi: 10.1109/access.2019.2947848
- 567 Murray, J. R., Crowell, B. W., Grapenthin, R., Hodgkinson, K., Langbein, J. O.,  
568 Melbourne, T., . . . Schmidt, D. A. (2018). Development of a Geodetic Compo-  
569 nent for the U.S. West Coast Earthquake Early Warning System. *Seismological*  
570 *Research Letters*, 89(6), 2322–2336. doi: 10.1785/0220180162
- 571 Nikolaidis, R. M., Bock, Y., Jonge, P. J. d., Shearer, P., Agnew, D. C., & Domse-  
572 laar, M. V. (2001). Seismic wave observations with the Global Positioning  
573 System. *Journal of Geophysical Research: Solid Earth*, 106(B10), 21897–  
574 21916. Retrieved from [https://agupubs.onlinelibrary.wiley.com/doi/](https://agupubs.onlinelibrary.wiley.com/doi/abs/10.1029/2001JB000329)  
575 [abs/10.1029/2001JB000329](https://agupubs.onlinelibrary.wiley.com/doi/abs/10.1029/2001JB000329) doi: 10.1029/2001jb000329
- 576 Ohta, Y., Kobayashi, T., Tsushima, H., Miura, S., Hino, R., Takasu, T., . . . Umino,  
577 N. (2012). Quasi real-time fault model estimation for near-field tsunami  
578 forecasting based on RTK-GPS analysis: Application to the 2011 Tohoku-  
579 Oki earthquake (Mw 9.0). *Journal of Geophysical Research: Solid Earth*  
580 (1978–2012), 117(B2), n/a–n/a. doi: 10.1029/2011jb008750
- 581 Pedregosa, F., Varoquaux, G., Gramfort, A., Michel, V., Thirion, B., Grisel, O., . . .  
582 Duchesnay, E. (2011). Scikit-Learn: Machine Learning in Python. *J. Mach.*  
583 *Learn. Res.*, 12(null), 2825–2830.
- 584 Psimoulis, P. A., Houlié, N., Habboub, M., Michel, C., & Rothacher, M. (2018). De-  
585 tection of ground motions using high-rate GPS time-series. *Geophysical Jour-*  
586 *nal International*, 214(2), 1237–1251. doi: 10.1093/gji/ggy198
- 587 Ruhl, C. J., Melgar, D., Geng, J., Goldberg, D. E., Crowell, B. W., Allen, R. M., . . .  
588 D’Anastasio, E. (2019). A Global Database of Strong-Motion Displacement  
589 GNSS Recordings and an Example Application to PGD Scaling. *Seismological*  
590 *Research Letters*, 90(1), 271–279. doi: 10.1785/0220180177
- 591 Shu, Y., Fang, R., Li, M., Shi, C., Li, M., & Liu, J. (2018). Very high-rate GPS  
592 for measuring dynamic seismic displacements without aliasing: performance  
593 evaluation of the variometric approach. *GPS Solutions*, 22(4), 121. doi:  
594 10.1007/s10291-018-0785-z
- 595 Smalley, R. (2009). High-rate GPS: How High Do We Need to Go? *Seismological*  
596 *Research Letters*, 80(6), 1054–1061. doi: 10.1785/gssrl.80.6.1054
- 597 van Graas, F., & Soloviev, A. (2004). Precise Velocity Estimation Using a Stand-

598 Alone GPS Receiver. *Navigation*, 51(4), 283–292. doi: 10.1002/j.2161-4296  
599 .2004.tb00359.x  
600 Wessel, P., Luis, J. F., Uieda, L., Scharroo, R., Wobbe, F., Smith, W. H. F., &  
601 Tian, D. (2019). The generic mapping tools version 6. *Geochemistry,*  
602 *Geophysics, Geosystems*, 20(11), 5556-5564. Retrieved from [https://](https://agupubs.onlinelibrary.wiley.com/doi/abs/10.1029/2019GC008515)  
603 [agupubs.onlinelibrary.wiley.com/doi/abs/10.1029/2019GC008515](https://agupubs.onlinelibrary.wiley.com/doi/abs/10.1029/2019GC008515) doi:  
604 <https://doi.org/10.1029/2019GC008515>

figure 1.

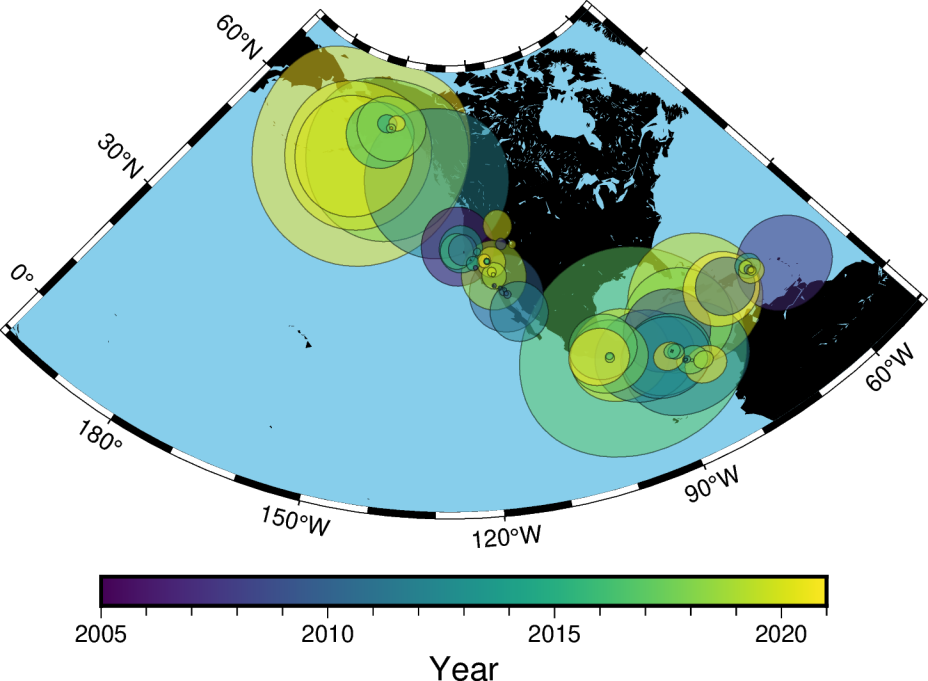


figure 2.

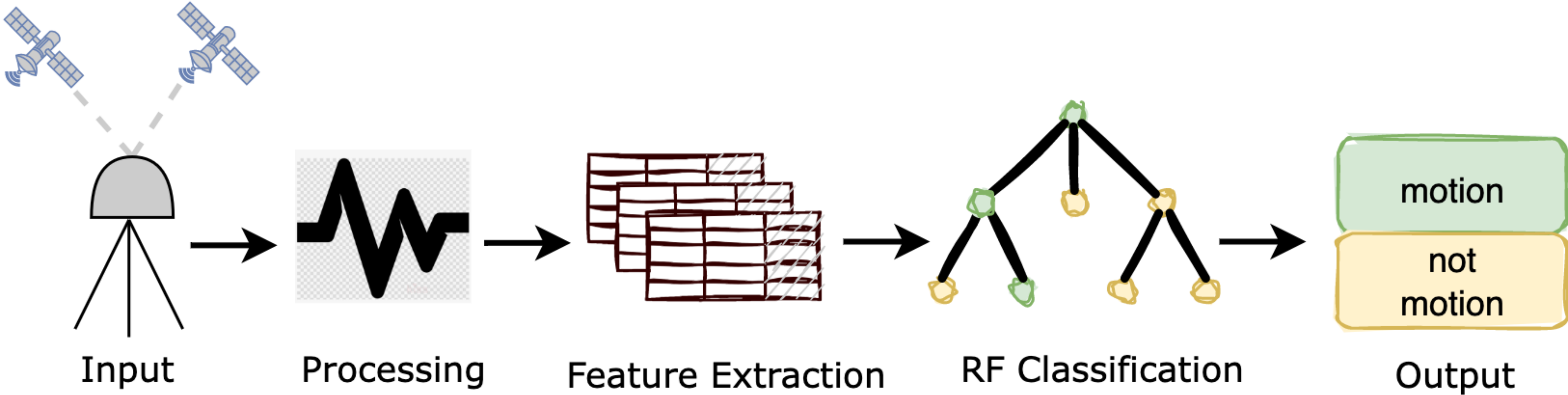
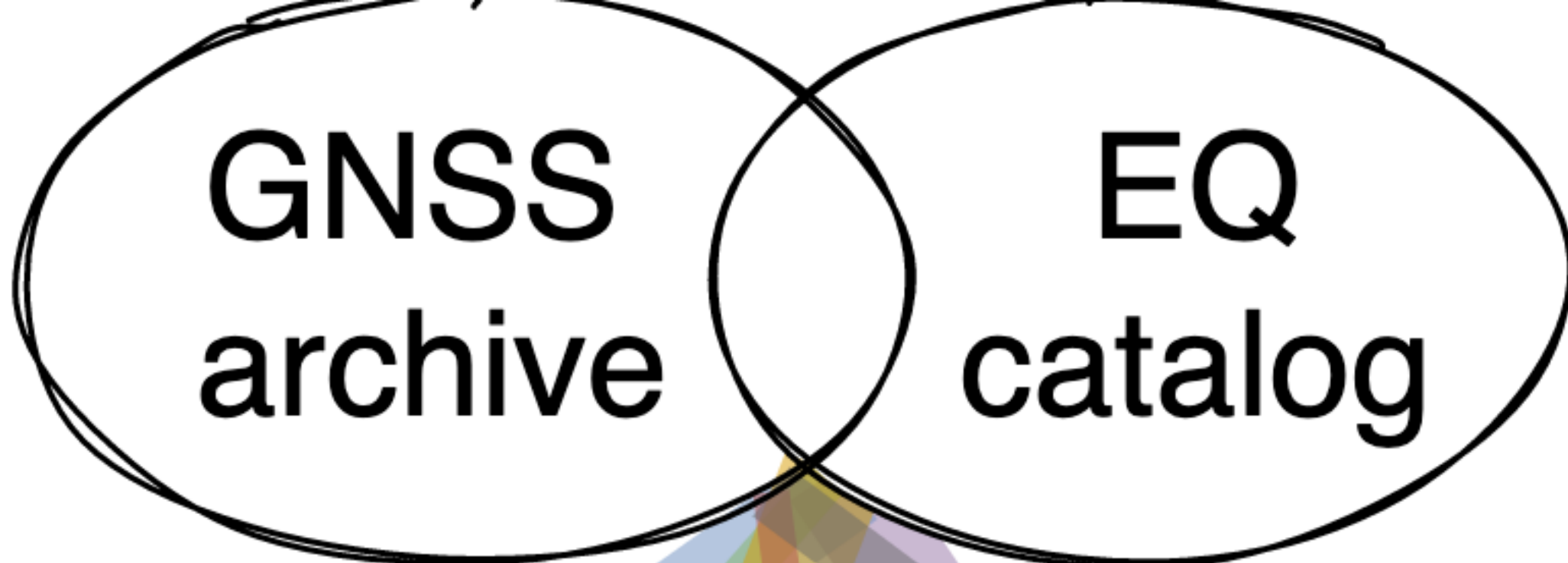


figure 3.

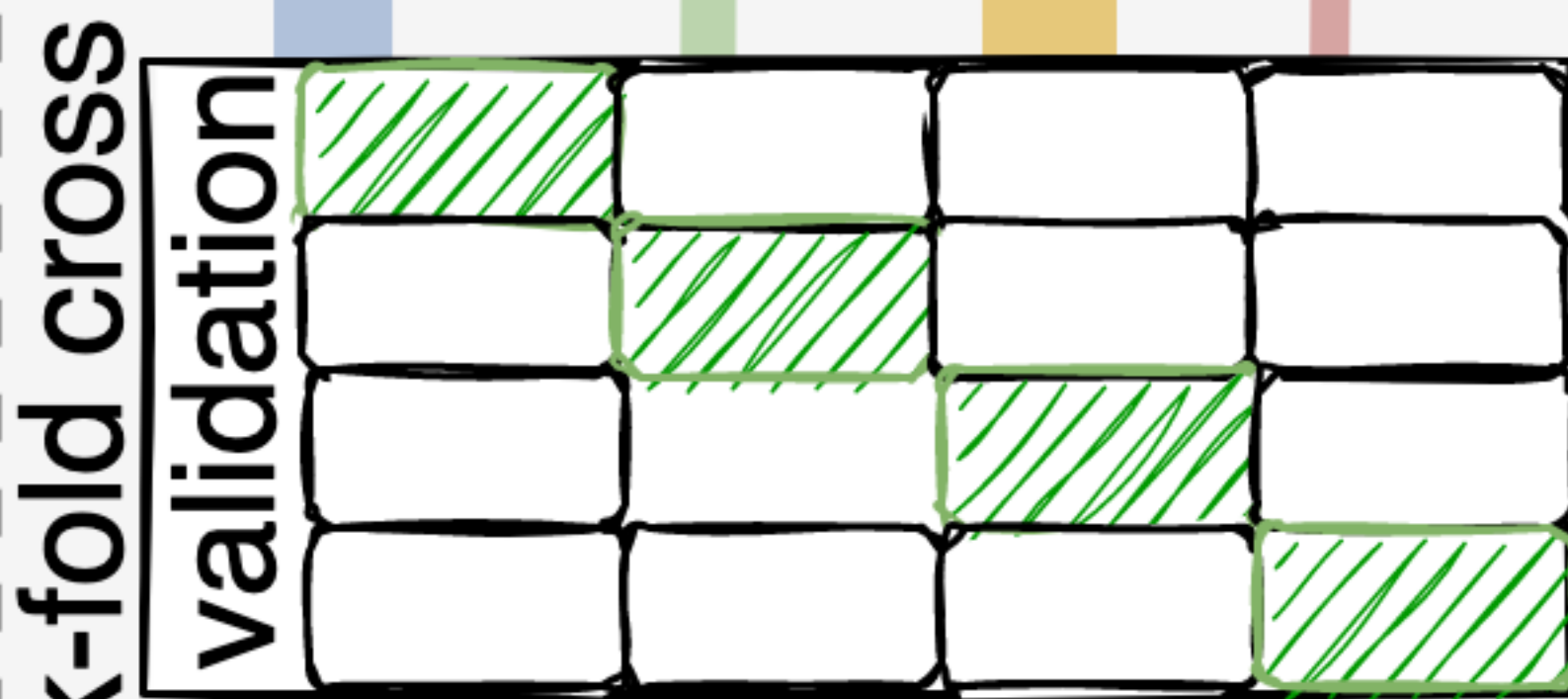


TDCP SNIVEL velocities

feature selection and class labeling

training  
*feature vectors*  
*target vectors*

testing  
*feature*  
*target*



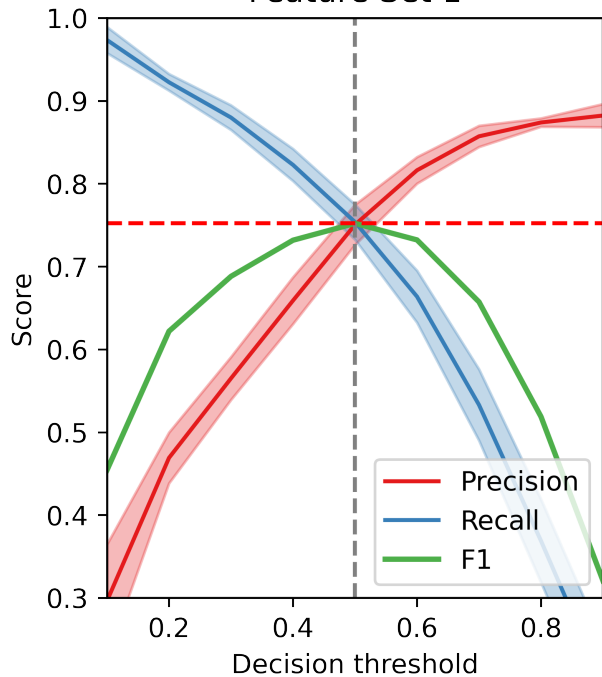
fit random forest model

test model

10 Fold Nested Cross Validation

figure 4.

Feature Set 1



Feature Set 2

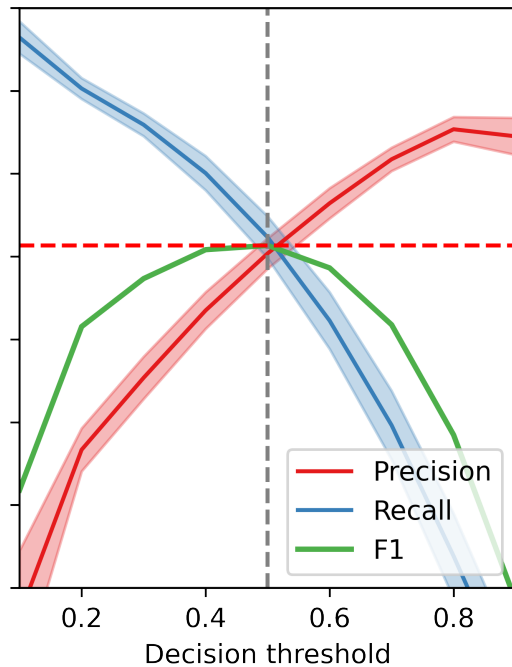


figure 5.

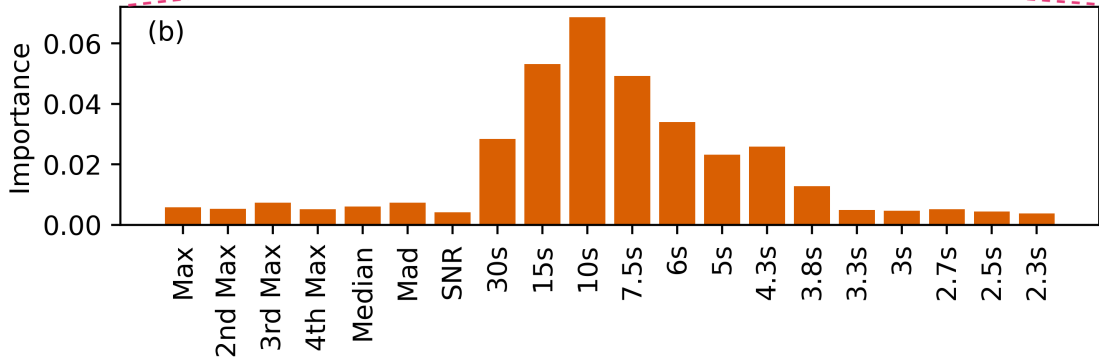
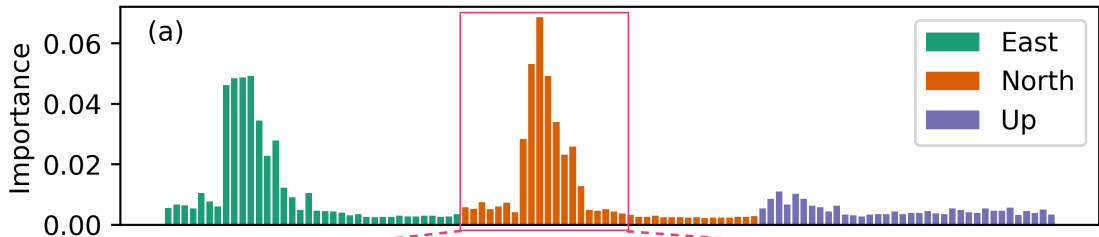


figure 6.

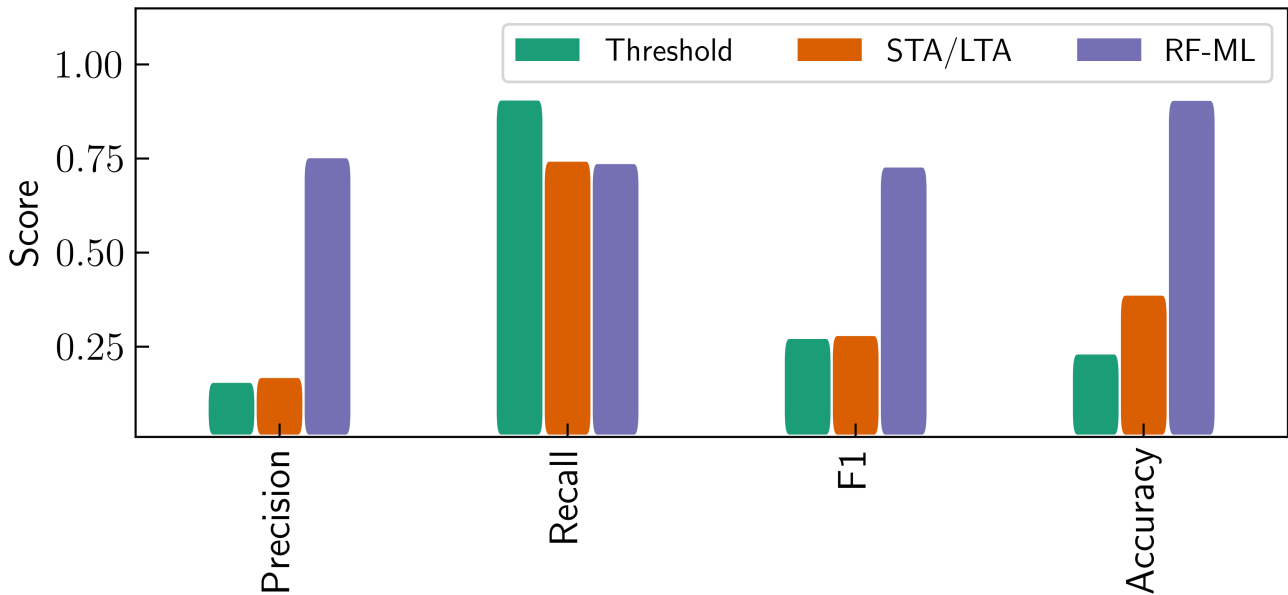


figure 7.

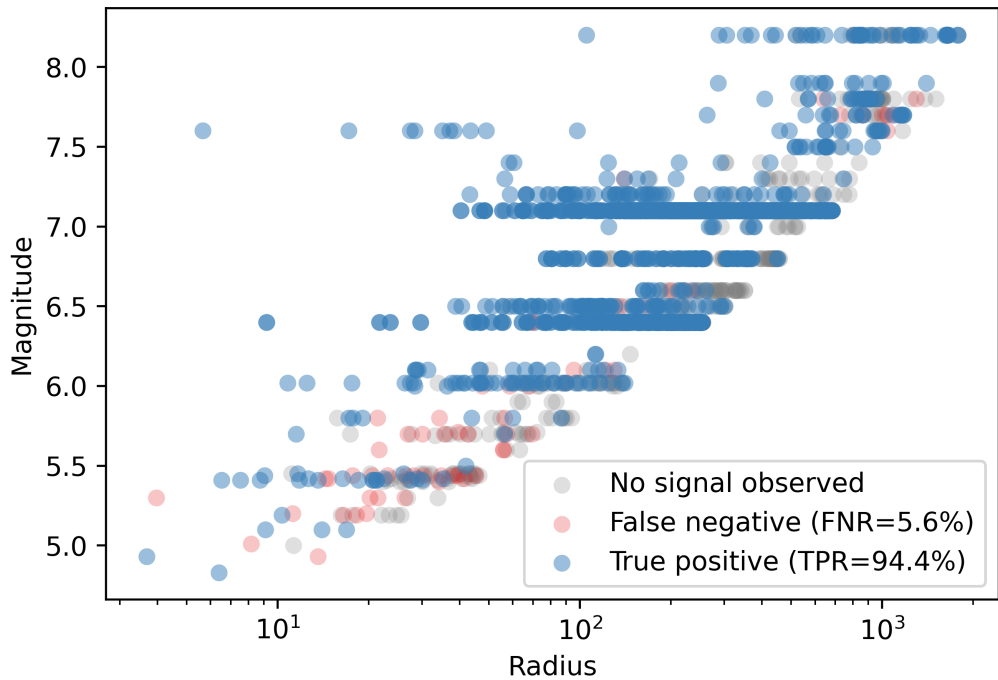
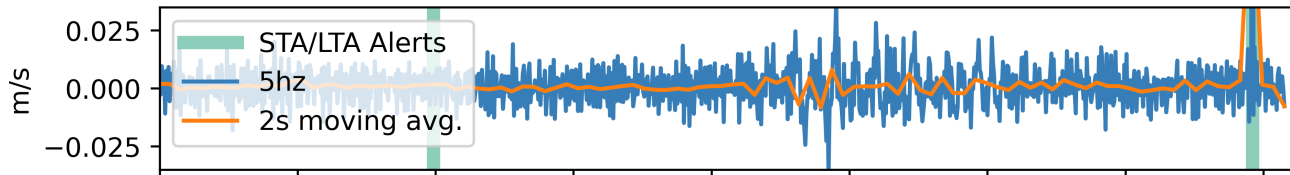
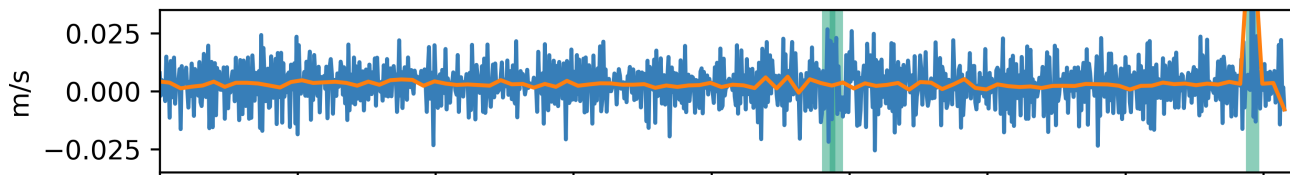


figure 8.

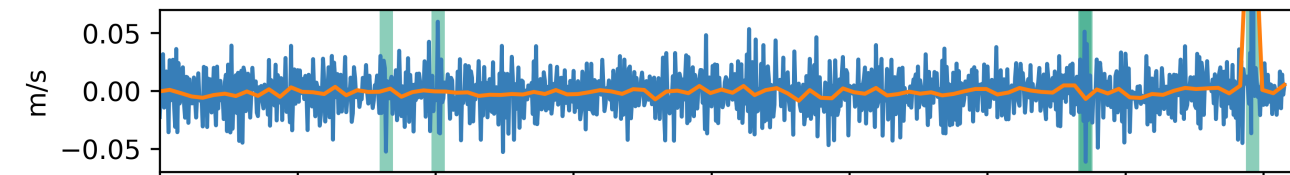
### East



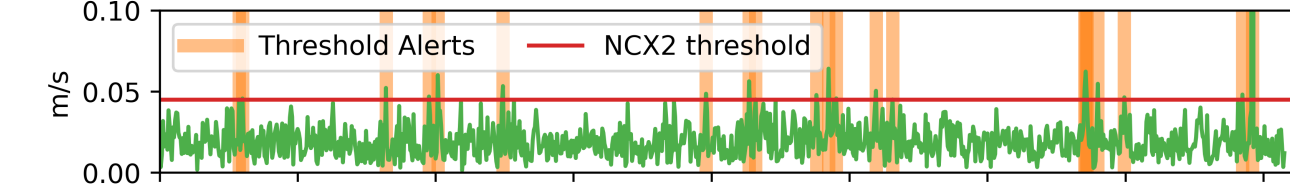
### North



### Vertical



### PGV



### Random Forest Classifier

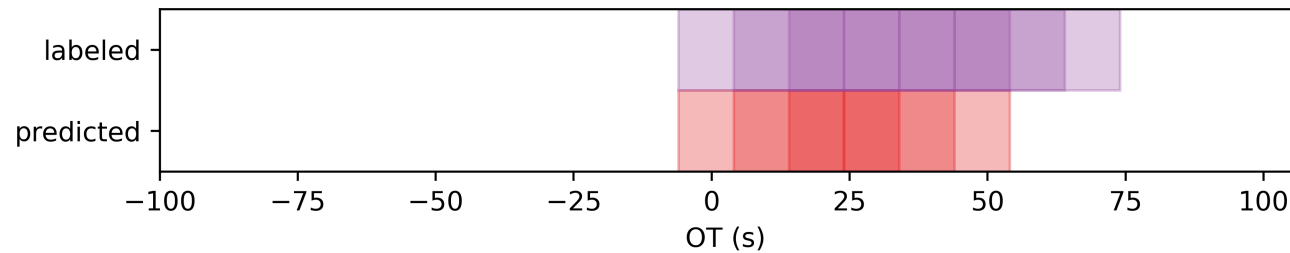


figure 9.

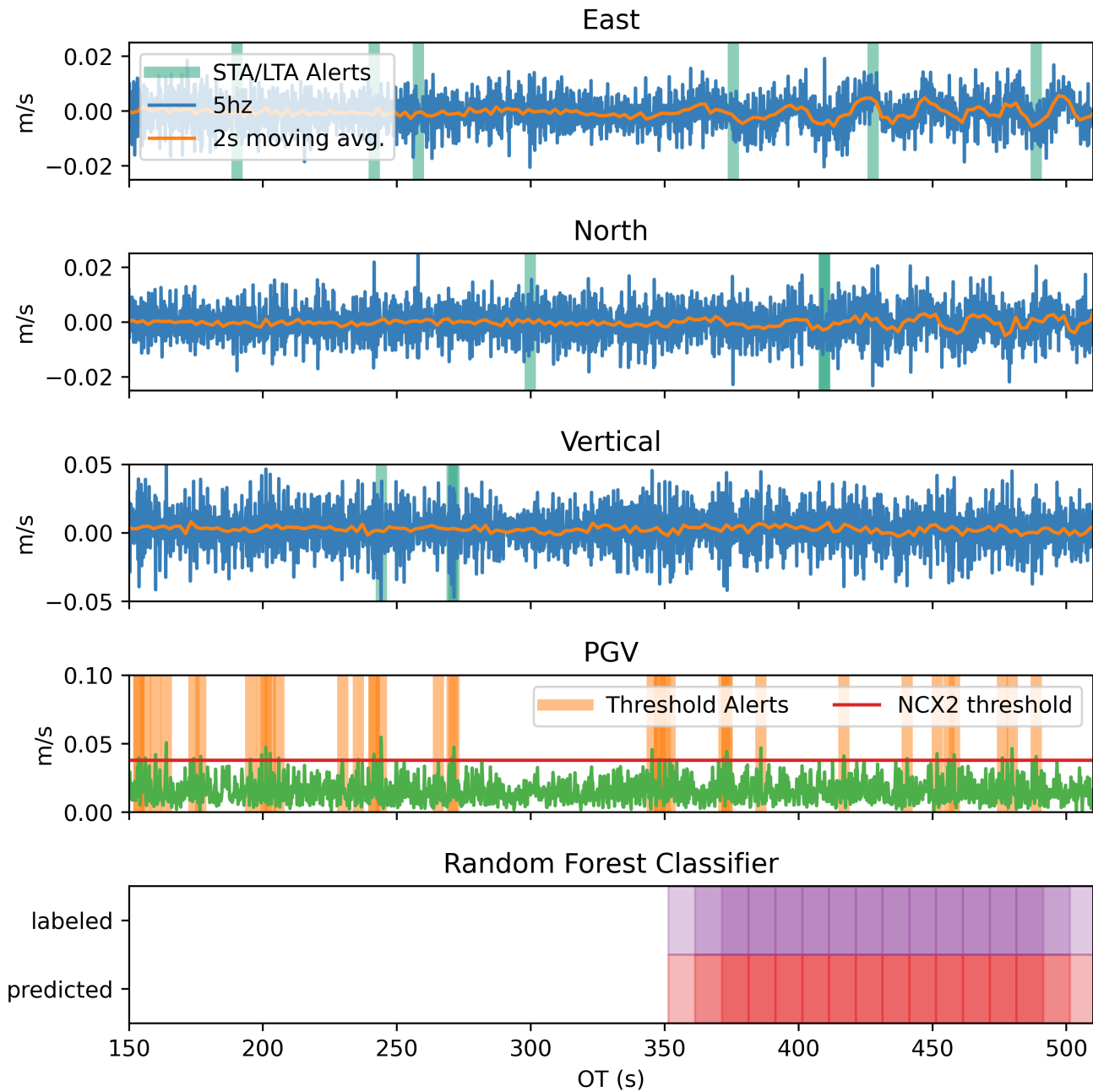


figure 10.

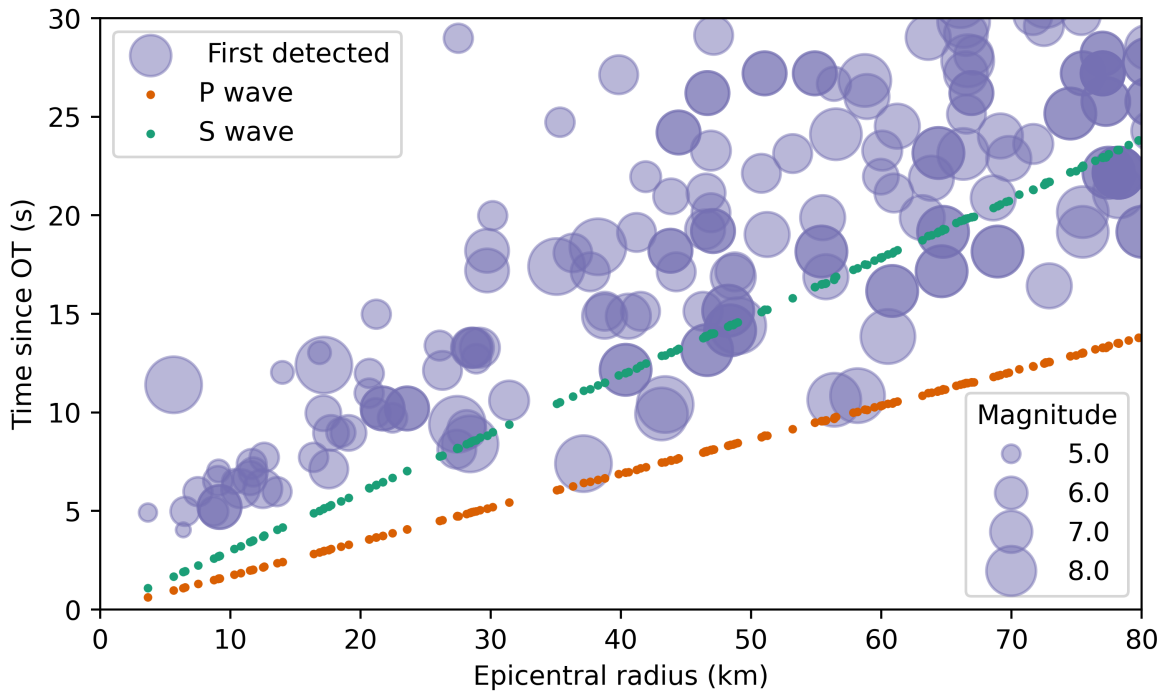


figure 11.

